Autoimmune regulator deficiency causes sterile epididymitis and impacts male fertility through disruption of inorganic physiology

Soo Hyun Ahn,[1] Katrina Halgren,[2] Geoffrey Grzesiak,[1] Keith W. MacRenaris,[3] Aaron Sue,[3] Huirong Xie,[4] Elena Demireva,[4] Thomas V. O'Halloran,[3,5,6*] and Margaret G. Petroff[1,6,7*]

*Corresponding Authors

Corresponding author email: petrof10@msu.edu

Affiliations

[1] Department of Pathobiology Diagnostic Investigation, College of Veterinary Medicine, Michigan State University, East Lansing, MI, USA.

[2]Lyman Briggs College, Michigan State University, East Lansing, MI, USA

[3]Elemental Health Institute and Department of Microbiology Genetics and Immunology, Michigan State University, East Lansing, MI, USA.

[4]Transgenic and Genome Editing Facility, Institute for Quantitative Health Science & Engineering, Research Technology Support Facility, Michigan State University, East Lansing, MI, USA

[5]Department of Chemistry, Michigan State University, East Lansing, MI, USA

[6]Institute for Integrative Toxicology, Michigan State University, East Lansing, MI, USA.

[7]Department of Microbiology, Genomics, and Immunology, Michigan State University, East Lansing, MI, USA

Funding: This research is supported by NIH grants R01 HD100832, R01 GM11484 and the National Research Resource for Quantitative Mapping in the life Sciences, supported by the Office of the Director, National Institutes of Health, and the National Institute for General Medical Sciences under grant number P41 GM135018.

23 **Running Title: Aire-deficiency disrupts inorganic physiology and leads to sterile**

24 **epididymitis**

25

26

27

Abstract

Autoimmune regulator (AIRE), a transcription factor expressed by medullary thymic epithelial cells, is required for shaping the self-antigen tolerant T cell receptor repertoire. Humans with mutations in *AIRE* suffer from Autoimmune Polyglandular Syndrome Type 1 (APS-1). Among many symptoms, men with APS-1 commonly experience testicular insufficiency and infertility, but the mechanisms causing infertility are unknown. Using an *Aire*-deficient mouse model, we demonstrate that male subfertility is caused by sterile epididymitis characterized by immune cell infiltration and extensive fibrosis. In addition, we reveal that the presence of autoreactive immune cells and inflammation in epididymides of *Aire*-deficient mice are required for iron (Fe) deposition in the interstitium, which is brought on by macrophages. We further demonstrate that male subfertility is associated with a decrease in metals zinc (Zn), copper (Cu), and selenium (Se) which serve as cofactors in several antioxidant enzymes. We also show increase in DNA damage of epididymal sperm of *Aire*$^{-/-}$ animals as a key contributing factor to subfertility. The absence of *Aire* results in autoimmune attack of the epididymis leading to fibrosis, Fe deposition, and Cu, Zn and Se imbalance, ultimately resulting in sperm DNA damage and subfertility. These results highlight the requirement of *Aire* to promote immune tolerance throughout the epididymis, disruption of which causes an imbalance of inorganic elements with resulting consequence on male fertility.

Key points:

Breakdown of epididymal self-tolerance promotes disruption of inorganic elements.

Autoimmunity causes interstitial fibrosis resulting in sperm DNA damage and subfertility.

Elevated interstitial iron and macrophages contribute to fibrosis.

Introduction

Infertility, a condition in which a couple is unable to achieve pregnancy after 12 months of unprotected intercourse, affects approximately 1 in 6 individuals worldwide, with lifetime prevalence ranging from 10.8 to 23.4% depending on global region.[1] Male factors are thought to account about 20% of cases, and contribute to as much as 60%.[2] Male infertility can stem from defective testicular function resulting in abnormal sperm concentration, motility, and morphology.[3] However, many cases of infertility are unexplained, occurring despite normal sperm parameters.[4] In these cases, underlying autoimmune disease may contribute by promoting inflammation of the reproductive organs, especially the epididymis,[5] which could perturb sperm maturation.

Autoimmunity, or loss of immune self-tolerance, results from inappropriate T cell reactivity towards self-antigens. Self-tolerance in T cells is established in the thymus through the expression of a transcription factor called Autoimmune Regulator (AIRE) by medullary thymic epithelial cells (mTECs). In these cells, AIRE regulates transcription of tissue-restricted antigens, which are then presented in the context of major histocompatibility complex; nascent autoreactive T cells that interact too strongly with the presented self-antigen are subsequently eliminated or directed into a regulatory phenotype.[6] In humans, mutation in the *AIRE* gene causes Autoimmune Polyglandular Syndrome Type 1 (APS-1), a rare autoimmune disease that manifests in a variety of symptoms including mucocutaneous candidiasis, hypoparathyroidism, adrenal insufficiency, gonadal insufficiency, and infertility.[7–9]

72 Using an Aire deficient (*Aire*$^{-/-}$) mouse model, we previously documented CD3+ T cell infiltration
73 into the prostate gland, seminal vesicles, epididymis, and more rarely, the testis.[10] In addition,
74 while sperm production and morphology appeared normal, sperm from *Aire*$^{-/-}$ males were severely
75 impaired in their ability to fertilize eggs. *In vitro* fertilization using *Aire*$^{-/-}$ epididymal sperm
76 resulted in only 9% of embryos reaching the 2-cell stage, and none reaching the blastocyst stage.[10]
77 These results suggest that malfunction of sperm in *Aire*$^{-/-}$ males are caused during post-
78 spermatogenic maturation in the epididymis, possibly due to abnormalities in the epididymal
79 environment.
80
81 The epididymis is an elongated, tightly coiled tube that connects each testicle to the vas deferens.
82 In addition to storing and transporting sperm in its distal-most portion (cauda) prior to ejaculation,
83 the epididymis provides important factors that transform the immature testicular sperm into
84 mature, fertilization-competent sperm.[11,12] The epididymis is indispensable for final post-testicular
85 maturation of sperm; if they do not traverse the entire length of the epididymis, they remain
86 incapable of fertilization.[13,14] The rodent epididymis is divided into four anatomical regions: the
87 initial segment (most proximal to the testis), the caput (head), the corpus (body), and the cauda
88 (tail) (most distal to the testis, merging into the vas deferens). With their distinct transcriptomic
89 profiles[15] and luminal contents,[16] each segment has specific roles in facilitating sperm maturation.
90 The epididymis preserves sperm in a dormant state by tightly regulating the pH of the lumen.[17,18]
91 Epididymal epithelial cells also produce antioxidant enzymes, including glutathione peroxidases,
92 perioxiredoxins, and superoxide dismutases, for which essential metals serve as requisite
93 cofactors.[12,19–21 22,23] Thus, any disruption in this epididymal environment may cause defects in
94 sperm maturation and their fertilization competence, ultimately resulting in infertility.

95

96 Here, we demonstrate that deletion of *Aire* promotes targeting of the epididymis by autoreactive
97 immune cells, resulting in epididymitis, interstitial fibrosis, dysregulation of inorganic physiology,
98 and severely compromising fertility. Using a range of emerging methods to determine quantitative
99 inorganic phenotypes,[24] we demonstrate that autoimmune-mediated epididymal damage results in
100 interstitial fibrosis and is associated with iron deposition, depletion of essential antioxidant
101 cofactors such as zinc (Zn), copper (Cu), and selenium (Se), and DNA damage of the sperm. By
102 crossing *Aire*$^{-/-}$ mice to mice deficient in T and B cells through deficiency in Recombination
103 Activating Gene 1 (Rag1), which plays a fundamental role in generating T and B cells, we also
104 demonstrate the role of the adaptive immune system in compromising fertility in *Aire*$^{-/-}$ males and
105 driving fibrinogenesis and inorganic physiology.

106

107 **Materials and Methods**

108 *Animals*

109 Experiments with animals complied with NIH's *Guide for the Care and Use of Laboratory*
110 *Animals*,[25] and were approved by the Institutional Animal Care and Use Committee at Michigan
111 State University. Mice were maintained on a 12h:12h light cycle with rodent chow (Teklad 2019;
112 Inotiv), which is formulated to support gestation in transgenic and inbred animals, and water
113 available *ad libitum*. Mice containing mutations in the autoimmune regulator (*Aire*) gene were
114 generated on the Balb/cJ background (Jackson Laboratories) by the Michigan State University
115 Transgenic and Genome Editing Facility using CRISPR/Cas9 targeting. A single guide RNA
116 (gRNA) targeting exon 2 of the *Aire* gene (**ENSMUSG00000000731**), with protospacer and PAM
117 sequence 5'- GAC GCT CCG TCT GAA GGA GA – AGG 3' (g158), was synthesized by IDT.

118 Ribonucleoprotein (RNP) complexes of Cas9 and gRNA were assembled and electroporated into
119 Balb/c zygotes to generate mutant mice as previously described.[26] Resulting edited founders
120 carrying 32 base-pair (bp), 44bp, or 86bp deletions were identified and backcrossed with Balb/c
121 mice to establish the transgenic lines. Preliminary findings showed profound male subfertility in
122 all three lines; data used in this manuscript were generated from the 32 bp line.
123
124 *Aire*$^{+/-}$ mice were crossed with *Rag1*-deficient animals to generate mice that were heterozygous for
125 both *Aire* and *Rag1* genes. Mice were genotyped by PCR analysis of tail biopsy genomic DNA
126 using the following primers: Aire F1: 5'-CAC ACC CTA TGC CCC CTA AC-3', Aire R1- 5`-
127 ACA TGG GCC GAC TTG TAT CC-3`; Rag1MutFwd: 5`-TGG ATG TGG AAT GTG TGC
128 GAG-3`; Rag1Common: 5`-TAC ACC TTG GCG ACG ACT CCT-3`, Rag1WTFwd: 5`-TCT
129 GGA CTT GCC TCC TCT GT-3`. *Aire*-deleted animals were confirmed for the absence of Aire
130 protein in the thymus by immunofluorescent staining, using wild type thymus as a control.
131
132 *Fertility trial*
133 6-week-old male *Aire*$^{+/+}$ (n=4) and *Aire*$^{-/-}$ (n=8) animals were paired with 6-week-old Balb/c virgin
134 females to assess fertility. These animals were either WT or heterozygous for the *Rag1* gene. To
135 assess the role of the adaptive immune system in fertility outcome of *Aire*$^{-/-}$ mice, additional
136 pairings of *Aire*$^{-/-}$*Rag1*$^{-/-}$ males (n=4) and *Aire*$^{+/+}$*;Rag1*$^{-/}$ males (n=3) were established. Mice
137 remained paired for 14.5 to 16 weeks, with the exception that two of the three *Aire*$^{+/+}$*;Rag1*$^{-/-}$ males
138 were paired for ~6 weeks. At the conclusion of the fertility trial, males were euthanized for
139 downstream analyses at 19 to 23 weeks of age; additional males were euthanized at 7-9 weeks.

140 Females were euthanized at the same time as the males, except when they were pregnant, in which
141 case they were euthanized following birth of the litter. Fertility rate was calculated as:

142 $$(number\ of\ litters \div number\ of\ days\ paired) \times 21$$

143 We chose 21 days as an expected length of mouse gestation; if dams produced a litter of pups
144 every 21 days, the resultant number would be close to 1.

145

146 *Histology*

147 Paraffin-embedded tissues were fixed in 4% paraformaldehyde at 4°C overnight, transferred to
148 70% ethanol, embedded in paraffin, and sectioned at 5 µm onto SuperFrost slides (Thermofisher
149 Scientific). Alternatively, tissues were fixed in 4% paraformaldehyde at 4°C overnight, transferred
150 to 30% sucrose, and embedded in OCT medium (Sakura) by freezing the medium in liquid-
151 nitrogen chilled isopentane. OCT-embedded samples were kept at -80°C until cryosectioning
152 (Leica Biosystems). For hematoxylin and eosin staining,[27] we used the Leica SelecTech staining
153 system consisting of Hematoxylin 560, Blue Buffer 8, Define, Alcoholic Eosin Y 515. Sections
154 were deparaffinized in Histoclear (National Diagnostics) and rehydrated in a gradient of ethanol
155 (100%, 95% and 80%) and water. Slides were stained in hematoxylin for 3 minutes, washed in
156 water for 1 minute, and immersed in 95% ethanol for 40 seconds followed by alcoholic eosin Y
157 for 12 seconds. Slides were then washed using two exchanges of 90% ethanol for 40 seconds and
158 dehydrated in 100% ethanol for 5 minutes. Finally, slides were washed in Histoclear for 5 minutes
159 and mounted using Cytoseal 60 (Fisher Scientific). For Masson's trichrome staining, which was
160 used to assess fibrosis, serially sectioned samples were submitted to the Investigative
161 Histopathology Core at Michigan State University. Using this stain, connective tissue stains blue,
162 nuclei stain purple/red, and cytoplasm stains pink/red.

163

164 *Immunohistochemistry and Immunofluorescence*

165 Paraffin-embedded epididymal tissue sections were immunohistochemically stained with rabbit
166 anti-CD8 (ab217344, Abcam), rabbit anti-CD4 (Abcam), rat anti-CD19 (6OMP31, Thermofisher
167 Scientific), rat anti-F4/80 (123102, Biolegend), or rabbit anti-αSMA (14395-1-AP, Proteintech)
168 antibodies. After deparaffinization and rehydration, we performed a heat-mediated antigen
169 retrieval step using Reveal Decloaker sodium citrate buffer (Biocare Medical), heated to 199°F for
170 20 minutes. After cooling to room temperature, samples were incubated with the SuperBlock™
171 blocking buffer (37515, ThermoFisher Scientific) for 10 minutes followed by 3% hydrogen
172 peroxide in methanol to quench endogenous peroxidase activity for 10 minutes. Sections were
173 washed with phosphate buffered saline (PBS) before incubating with the primary antibody.
174 Adjacent sections were used for isotype controls. Biotinylated anti-rabbit or anti-rat IgG secondary
175 antibody (Vector Laboratories) was applied, followed by Ready-To-Use Horseradish Peroxidase
176 and DAB (Vector Laboratories) for color development.

177

178 To quantify positively stained cells, slides were scanned using a Zeiss Axioscan 7 Microscope
179 Slide Scanner (Carl Zeiss AG). Three nonoverlapping, randomly chosen regions of interest (ROI;
180 350 μm × 950 μm) were from the caput, corpus, and cauda epididymides were captured using Zen
181 Microscopy Software (Carl Zeiss). In some animals, only two non-overlapping regions could be
182 imaged. Three independent blinded evaluators counted DAB+ cells from slides stained with anti-
183 CD4 and anti-CD8 antibodies. The non-parametric Wilcoxon's t-test was used to compare the
184 means of DAB+ cells between *Aire*$^{+/+}$ and *Aire*$^{-/-}$ samples. Intraclass Correlation Coefficient was
185 used to assess the strength of inter-evaluator agreement and was calculated using the "icc" R

186 package. The ICC for this experiment was 0.91, indicating a high similarity between values
187 measured by the three independent evaluators.
188
189 For immunofluorescence, OCT-embedded samples were sectioned at 5 µm, washed in PBS
190 for 10 minutes, blocked using SuperBlock Blocking Buffer, and incubated overnight with
191 antibodies against F4/80, CD163 (1:400; Abcam), and/or Ferritin (1:1000; F5012, Sigma Aldrich).
192 The following day, the slides were washed and incubated with secondary antibodies (AF488-anti-
193 rat or AF546-anti-rabbit IgG; 0.01mg/mL, ThermoFisher Scientific) and mounted using ProLong
194 Gold antifade reagent with DAPI (ThermoFisher Scientific).
195
196 *Flow cytometry*
197 For flow cytometeric analysis of lymphocytes, epididymides from 2 males were pooled into 1
198 sample, such that 1 biological replicate consisted of cells from 2 males and 4 epididymides. Once
199 excised, cauda epididymides were dissected from the rest of the epididymis and collected into
200 TYH media warmed to 37°C to allow sperm to swim out of the sample. Cauda epididymides were
201 further processed and analyzed separately from caput-corpus epididymides such that spatial
202 information could be maintained while ensuring sufficient cellular yield. Tissues were finely
203 minced using spring scissors, collected into gentleMACS™ M Tubes (Miltenyi Biotec), and
204 incubated in 5 mL of Miltenyi Tissue Dissociation Kit 1 (Miltenyi Biotec) for 15 minutes at 37°C,
205 using GentleMACS™ Dissociator (Miltenyi Biotec) for 1 minute per sample at room temperature.
206 The samples were returned to 37°C to incubate for a 15 additional minutes. The digest was filtered
207 through a 70 µm filter into 50 mL conical tubes containing 10 mL of PBS with 5% FBS to
208 neutralize the digestive enzyme. Each sample was topped up to 30 mL with 5% FBS and

209 centrifuged at 400g for 5 minutes. The cell pellet was washed with 10 mL of PBS/5%FBS buffer,
210 resuspended in 0.4 mL of PBS/5%FBS buffer, and aliquoted into 96 well plates for staining. All
211 cells were incubated with a viability stain (1:1000; Invitrogen™ Live/Dead™ Fixable Blue Dead
212 Cell Stain kit, ThermoFisher Scientific) for 30 minutes on ice, followed by staining with Mouse
213 BD FcBlock™ (1:100, 553142BD Pharmingen, Cat. No.) for 20 minutes on ice. Cells were
214 pelleted and resuspended with the primary antibody cocktail on ice for 30 minutes. The following
215 antibodies were used: BV421 anti-CD45 (1:200; 103133, 30-F11, Biolegend,), KIRAVIA Blue
216 520 anti-CD4 (1:100, clone GK1.5; Biolegend), BV785 anti-CD8 (1:100, 53-6.7, Biolegend), PE-
217 Dazzle 594 anti-CD44 (1:100, IM7, Biolegend), PE-Cy5 anti-CD69 (1:50; H1.2F3, Biolegend),
218 APC anti-CD25 (1:50; PC61, Biolegend), BV510 anti-B220 (1:100; RA3-6B2, Biolegend). After
219 incubation with primary antibodies, the cells were washed three times in 200 µL of flow staining
220 buffer, pelleting the cells between each wash. Lastly, cells were fixed using 1% paraformaldehyde
221 in PBS for 15 minutes on ice and stored at 4°C until analysis using Cytek® Aurora spectral flow
222 cytometer (Cytek® Biosciences,).
223
224 *Gelatin standard preparation*
225 Gelatin standards (blank, 1, 5, 10, 20, 50 parts per million (ppm)) (**Supplemental Table 1**) were
226 produced by mixing in IV-Stock-4 (Inorganic Ventures) to 10% porcine gelatin (G2500-500G,
227 Sigma Aldrich) and heated to 55°C. The blank contained no IV-Stock-4. 400 µL of the preparation
228 was pipetted directly onto the cryostat mounting chuck, left to freeze at -20°C for 4 minutes, and
229 sectioned at 20 µm thickness onto the SuperFrost glass slides (Thermofisher Scientific). A 50 µL
230 aliquot of each standard was aliquoted in a pre-weighed metal-free tube to determine elemental
231 concentrations using an Agilent 8900 Triple Quadrupole - Inductively Coupled Plasma - Mass

232 Spectrometer (ICP-QQQ-MS, Agilent) equipped with the Agilent SPS 4 Autosampler, integrate
233 sample introduction system (ISiS), x-lens, and micromist nebulizer. To each sample, 300 µL of
234 trace metal grade 70% nitric acid (Fisher chemical, #A509P212), was added to digest the sample
235 at 70 °C for 4 hours. Following digestion, 9.7 mL of ultrapure deionized water was added to each
236 sample. All samples were weighed prior to analysis on the ICP-QQQ-MS.
237
238 *Spatial, quantitative mapping element distribution using LA-ICP-TOF-MS*
239 Paraffin-embedded 5 µm tissue sections were mounted onto charged glass slides and laser ablated
240 using the Elemental Scientific Lasers BioImage 266 nm laser ablation system (Elemental Scientific
241 Lasers), which is equipped with an ultra-fast low dispersion TwoVol3 ablation chamber and a dual
242 concentric injector (DCI3). The aerosolized sample was transferred to the Tofwerk icpTOF S2
243 mass spectrometer (TOFWERK AG) where the elemental content was analyzed real time
244 according to mass/charge (m/z) ratio. Daily tuning was performed using NIST SRM612 glass
245 certified reference material (National Institute for Standards and Technology). High intensities for
246 ^{140}Ce and ^{55}Mn were used to optimize torch alignment, lens voltages, and nebulizer gas flow while
247 maintaining low oxide formation based on the ^{232}Th^{16}O+/^{232}Th+ ratio (< 0.5). Parameters are listed
248 in **Supplemental Table 2**. Laser scanning was performed in a raster pattern with a laser repetition
249 rate of 100 Hz using a 10 µm circular spot size with laser fluence set to 15 J/cm^2. Ten lines of
250 gelatin standards were ablated using the same parameters but with the raster spacing set at 20 µm.
251 Scanning data was recorded using TofPilot 1.3.4.0 (TOFWERK AG) and saved in the open-source
252 hierarchical data format (HDF5). Post-acquisition data processing was performed with Tofware
253 v3.2.0, a data analysis package used as an add-on to IgorPro (Wavemetric Inc.). Imaging and mass
254 calibration was conducted using the Iolite version 4.8.6. Software (Elemental Scientific Lasers) .[28]

255

256 *Elemental Composition Determination by ICP-QQQ-MS*

257 Mouse epididymides separated into caput, corpus, and cauda were placed into a pre-weighed
258 metal-free 15mL conical tubes (Labcon) to be analyzed using ICP-QQQ-MS (Agilent). Prior to
259 analysis, each metal-free tube was weighed using an analytical balance pre- and post-addition of
260 the tissue sample to ascertain the weight of the tissue. Tissues were digested in 300 µL of 70%
261 nitric acid (Fisher, #A509P212) and incubated at 65°C overnight. The following day, 9.7 mL of
262 ultrapure deionized water was added to bring the final nitric acid concentration to 3% by volume.
263 Each tube was weighed again before analysis to ascertain the final weight of the sample. Standards
264 were prepared using IV-Stock-4 (Inorganic Ventures) at 0.01, 0.1, 1, 10, and 100 parts per billion
265 (ppb) using 3% nitric acid in metal-free 15 mL conical tubes. The element concentrations of the
266 samples were calculated using the following equation:

267 $$ug/g\ (ppm)\ =\ (weight\ of\ the\ ICP\ sample\ (g)\ *\ (0.001$$

268 $$*\ ppb))\ /\ weight\ of\ the\ sample\ (g)$$

269

270 *Comet assay*

271 The assay was conducted using the CometAssay® Single Cell Gel Electrophoresis Assay kit
272 (Catalog # 4250-050-K, R&D Systems). Cauda epididymides were collected from *Aire*$^{+/+}$ and
273 *Aire*$^{-/-}$ males into a 1.5 mL tube filled with 250 µL of PBS, gently minced with spring scissors, and
274 incubated for 15 minutes at 37°C to allow the sperm to swim out of the tissue. The supernatant
275 was collected into a separate 1.5mL centrifuge tube and counted using a hemocytometer by mixing
276 5 µL of the suspension with 95 µL of MilliQ water. Fifty µL of the resuspended sperm (1 million
277 cells/mL) were mixed with 500 µL of 1% LMAgarose, spread onto a glass slide, and placed at 4°C

278 for 30 minutes. The samples were then incubated with lysis buffer + Proteinase K (500 µg/mL) for
279 18 hours at 4°C. The following day, the slides were immersed in cold Neutral Electrophoresis
280 Buffer (0.5M Tris-HCL, 1.5M sodium acetate) and subjected to electrophoresis at 21V/cm for 45
281 minutes at 4°C. Next, the slides were immersed in DNA Precipitation Solution and immersed in
282 70% ethanol for 30 minutes each at room temperature. The slides were dried at 37°C and stained
283 with 100 uL of SYBR® Gold Nucleic Acid Gel stain (1:10000, S11494, ThermoFisher Scientific)
284 for 30 minutes at room temperature. Lastly, the slides were briefly washed in tap water, dried, and
285 imaged using a 488 nm filter (Zeiss Axioscan 7). To calculate the percentage of sperm with comet
286 tails, Fiji software was used to convert the images to 8-bit, and threshold was set between 65-70
287 range to 255, followed by the "Analyze Particle" function in Fiji, which counted the number of
288 sperm heads (particle size set to 10 - 250) present on the image. To calculate proportion of sperm
289 with fragmented DNA, the comet tails were manually counted from the same image, divided by
290 the total number of particles detected, and multiplied by 100.
291
292 *Statistical analysis*
293 R studio and the packages ggplot2, ggbeeswarm, readxl, ggpubr, ggsci, icc, and tidyverse were
294 used to generate graphs and conduct statistical analysis. Normal distribution of the data was tested
295 using the Shapiro-Wilks test. For comparison of the means between two independent, normally
296 distributed samples, Student's t-test was used; for more than two, one-way ANOVA followed by
297 Tukey's post-hoc test was used. For samples that failed Shapiro-Wilks normality test, Wilcoxon's
298 test was used to compare the means of two samples, and Kruskal-Wallis test for two or more
299 samples, followed by Dunn's post-hoc test. For the comet assay, a paired t-test was conducted. *P*-
300 values less than 0.05 were deemed statistically significant.
301

302 **Results**

303 ***Aire*$^{-/-}$ males subfertility is dependent on the adaptive immune system**

304 We generated transgenic animals heterozygous for *Aire* and *Rag1* genes on the Balb/c background.
305 The absence of *Rag1* gene with *Aire*-deficiency (*Aire*$^{-/-}$) produces animals without adaptive T and
306 B cells (*Aire*$^{-/-}$;*Rag1*$^{-/-}$), allowing us to address the role of central tolerance to male reproductive
307 tissues. Since we rederived the *Aire*$^{-/-}$ animals using CRISPR/Cas9, we validated the absence of
308 Aire protein in the thymus using immunofluorescence **(Fig 1A)**. We also tested whether the *Aire*$^{-}$
309 $^{/-}$ animals recapitulated the development of autoimmunity and infertility, as previously
310 demonstrated by us and others.[6,10,29] We observed immune cell infiltration in both reproductive
311 and non-reproductive organs (**Fig. 1B**), confirming that our *Aire*$^{-/-}$ mouse model recapitulated
312 established mouse models of APS-1.[6] Because we observed smaller testes with immune cell
313 infiltration in about 14% of *Aire*$^{-/-}$ males examined,[10] we euthanized 10- and 20-week-old *Aire*$^{-/-}$
314 males to assess testicular histology. Hematoxylin and eosin staining showed normal seminiferous
315 tubules with intact spermatogenesis, comparable to *Aire*$^{+/+}$ testes in a majority of our *Aire*$^{-/-}$
316 samples at 10 weeks of age (*Aire*$^{+/+}$; n=4, *Aire*$^{-/-}$; n=4) and 20 weeks of age (*Aire*$^{+/+}$; n=9, *Aire*$^{-/-}$;
317 n=10, data not shown), suggesting that testes were not targeted by immune cells, or that the testes-
318 blood-barrier prevented immune cell infiltration in these *Aire*$^{-/-}$ mice.

319

320 To test fertility, 6-week-old *Aire*$^{+/+}$ (n=3) or *Aire*$^{-/-}$ (n=7), which were either heterozygous or wild-
321 type for the *Rag1* gene, were singly housed with virgin WT Balb/c females. Additionally, fertility
322 of *Aire*$^{+/+}$;*Rag1*$^{-/-}$ (n=3) and *Aire*$^{-/-}$;*Rag1*$^{-/-}$ (n=4) males was evaluated. Wild type (*Aire*$^{+/+}$*Rag1*$^{+}$)
323 males demonstrated robust fertility, with an average delivery rate of 0.85 litters per 21 days and
324 74 pups total over ~14 weeks. In contrast, the *Aire*$^{-/-}$;*Rag1*$^{+}$ males had an average delivery rate of
325 0.08 litters per 21 days, with only 17 total pups produced. The two litters produced by the seven

326 *Aire*$^{-/-}$ males occurred in the first 7 weeks of pairing, whereas *Aire*$^{+/+}$ males were able to sire litters
327 for the entire duration of pairing. *Aire*$^{-/-}$*;Rag1*$^{-/-}$ males showed fertility comparable to *Aire*$^{+/+}$ mice
328 **(Fig. 1C),** showing that adaptive immune cells are responsible for subfertility in *Aire*$^{-/-}$
329
330 ***Aire*$^{-/-}$ epididymides show immune cell infiltration**
331 Because the testis of *Aire*$^{-/-}$ mice appeared normal, we focused our attention on the epididymis,
332 where the testicular sperm undergo maturation, gain fertilization competency, and are stored
333 before ejaculation. Histological analysis of 10 and 20-week-old *Aire*$^{-/-}$ epididymides revealed
334 thickening of the interstitium and immune cell infiltration consisting of CD4+ and CD8+ T cells,
335 and CD19+ B cells **(Fig. 1B, 2A).** To measure the degree of infiltration of T cells, we counted the
336 immunohistochemically stained cells, with attention to age-dependent variation and differences
337 between the epididymal caput (head), corpus (body), and cauda (tail) (**Fig. 2B**). While CD4 and
338 CD8 cells in *Aire*$^{+/+}$ epididymides were found only sporadically, both cell types were frequently
339 found in *Aire*$^{-/-}$ mice in all three segments of *Aire*$^{-/-}$ animals in both young and old animals. No
340 differences between regions of epididymis within each strain were observed (P>0.05). Age-
341 dependent differences were not obvious, therefore data from young and aged animals were
342 combined. T cell infiltration of all three epididymal regions of *Aire*$^{-/-}$ mice were significantly
343 higher than those of *Aire*$^{+/+}$ mice (**Fig. 2C, D**). As expected, neither T nor B cells could be
344 identified in *Rag1*-deficient mice, regardless of absence or presence of *Aire* (not shown).
345
346 To characterize the activation status of the infiltrating epididymal T cells, we performed flow
347 cytometry, separating the caput and corpus from the cauda epididymides. Within genotype, no
348 differences were observed in the relative abundance of CD45hi immune cells in the different

349 regions of the epididymis (P>0.05). Between genotypes, the proportion of CD45hi cells among
350 total cells trended towards increasing in the corpus-caput, and significantly increased in the cauda
351 epididymis, of *Aire*$^{-/-}$ mice as compared to *Aire*$^{+/+}$ controls (**Fig. 3B**). Similarly, the proportion of
352 B cells remained similar within genotype, but increased in the cauda epididymis of *Aire*$^{-/-}$ mice
353 (**Fig. 3C**). Relative abundance of CD4+ and CD8+ T cells was higher in the epididymal caput-
354 corpus of *Aire*$^{-/-}$ mice than that of *Aire*$^{+/+}$ controls (**Fig. 3D, E**). In the cauda epididymis, CD4+ T
355 cells remained similar between knockout and control mice (**Fig. 3F**), but CD8+T cells increased
356 approximately 6-fold in *Aire*$^{-/-}$ mice **(Fig. 3G)**. Finally, the early activation marker CD69 was
357 elevated on CD8+ T cells of both caput-corpus (**Fig. 3E**) and cauda (**Fig. 3G**); in CD4+ T cells,
358 the CD69 expression appeared to increase but this did not reach statistical significance, possibly
359 due to insufficient statistical power (**Fig. 3D, F**). Nearly all CD4+ and CD8+ T cells were CD44^{high},
360 indicating prior antigen experience; levels of CD44, however, were unchanged between genotypes
361 (**Fig. 3D-G**). CD25 expression was also unchanged bewteen *Aire*$^{-/-}$ and *Aire*$^{+/+}$ mice, except for
362 CD4+ cells obtained from cauda epididymis (**Fig. 3F**). Few CD8+ T cells in either genotype
363 expressed IL-2Rα/activation marker CD25 (**Fig3. E, G**).
364

365 **^{56}Fe is increased in *Aire*$^{-/-}$ epididymis and correlates with fibrosis**

366 Thickening of the epididymal interstitium in *Aire*$^{-/-}$ mice (**Fig. 1B**) could indicate fibrotic change
367 of the tissue. To test this, tissues were stained with Masson's trichrome, which revealed increased
368 presence of collagen fibers in *Aire*$^{-/-}$ epididymides **(Fig. 4)**. We also probed for αSMA+
369 myofibroblast using immunohistochemistry, which are pertinent to fibrogenesis and scar
370 formation[30] (**Supplemental Fig. 1**). These cells were abundant in the interstitium of *Aire*$^{-/-}$
371 epididymis compared to *Aire*$^{+/+}$, indicating their potential involvement in fibrogenic

372 transformation of the interstitium in our *Aire*$^{-/-}$ animals. The epididymis of the age-matched *Aire*$^{-/-}$*;Rag1*$^{-/-}$ animals, which possess innate immune cells but lack mature T and B lymphocytes, did not develop fibrosis (**Fig. 4, third column)**, demonstrating that autoreactive adaptive immune cells are required to promote fibrogenesis of the epididymis.

376

377 Dysfunction in iron metabolism and homeostasis can cause hemochromatosis and idiopathic pulmonary fibrosis, both of which are characterized by extensive fibrotic changes of the organ.[31,32] To determine whether iron accumulation contributed to fibrosis in *Aire*$^{-/-}$ epididymis, we dissected the epididymis into its anatomically distinct regions **(Fig. 2B)** and used ICP-QQQ-MS for elemental quantification. Using this method, we found that ^{56}Fe concentration (µg/g tissue) regardless of age was elevated throughout the epididymis from *Aire*$^{-/-}$ males compared to *Aire*$^{+/+}$ and *Aire*$^{-/-}$*;Rag1*$^{-/-}$ **(Fig. 5A)**. In *Aire*$^{+/+}$ epididymides, the mean concentration of ^{56}Fe was comparable between caput, corpus, and cauda (21.5 ± 5.2 µg/g; 26.8 ± 10.1 µg/g; 29.8 ± 4.9µg/g, respectively). However, in *Aire*$^{-/-}$ epididymides, concentrations were 3-4-fold higher (caput, 69.8 ± 51.3 µg/g; corpus, 110.1 ± 35.7 µg/g; cauda, 85.2 µg/g ± 16.0 µg/g). The ^{56}Fe concentration in each of the epididymal segments of the *Aire*$^{-/-}$*;Rag1*$^{-/-}$ tissues were comparable to *Aire*$^{+/+}$ tissues and values were not significantly different (**Fig. 5A)**. ^{56}Fe concentration in the caudal sperm fraction was similar between *Aire*$^{+/+}$ and *Aire*$^{-/-}$, suggesting that increased ^{56}Fe is localized to the tissue rather than the sperm **(Fig. 5B).**

391

392 To visualize the spatial distribution of iron in the epididymis, we used laser ablation – inductively coupled plasma – time of flight – mass spectrometry (LA-ICP-TOF-MS) **(Fig. 5C**). Analogous to the spatial single-cell RNA sequencing that illuminates transcriptomics of a sample on a per-pixel

395 basis, LA-ICP-TOF-MS can delineate the total elemental content of a sample and instantaneously
396 allow spatial visualization of all elements within the periodic table in the tissue sample. Using this
397 technique, we found that ^{56}Fe was especially concentrated within the interstitium of the corpus and
398 cauda regions of both the young and the aged *Aire*$^{-/-}$ epididymides; this was not observed in either
399 *Aire*$^{+/+}$ or *Aire*$^{-/-}$*;Rag1*$^{-/-}$ tissues **(Fig. 5C).**
400

401 **F4/80+ macrophages are sources of ^{56}Fe in the interstitium**

402 We next asked what cells the excess iron originates from in *Aire*$^{-/-}$ epididymides. Because of known
403 associations between macrophages and iron in fibrosis of the lung,[33] we hypothesized that these
404 cells are a source of iron. We first used a macrophage-specific marker, F4/80, to characterize the
405 distribution of macrophages in the epididymis of *Aire*$^{+/+}$, *Aire*$^{-/-}$ and *Aire*$^{-/-}$*;Rag1*$^{-/-}$ animals using
406 immunohistochemistry (**Fig. 6A**). In the control tissues, F4/80+ macrophages were found as small,
407 densely stained cells in the interstitium of the epididymis. In *Aire*$^{-/-}$ tissues, macrophages became
408 elongated and were found throughout the interstitium of *Aire*$^{-/-}$ epididymis (**Fig. 6A),**
409 corresponding with the locations of fibrosis and iron accumulation (**Fig. 4, Fig. 5**). F4/80+
410 macrophages found within fibrotic regions of the epididymis were also CD163+ (**Fig. 6B**), a
411 marker commonly used to identify alternatively activated macrophages with profibrotic
412 transcriptomic signatures.[34] Collectively, the results suggest that macrophages with a pro-fibrotic
413 phenotype contribute to interstitial fibrosis in the *Aire*$^{-/-}$ epididymis.
414

415 Due to the ability of macrophages to store iron in the form of ferritin and hemosiderin, we asked
416 whether iron co-localized with F4/80+ macrophages. Indeed, we found that ferritin, a 24-mer iron
417 storage protein,[35] often co-localized with F4/80-positive macrophages, particularly in Aire$^{-/-}$

418 animals (**Fig. 6C**). Interestingly, in wild type animals, ferritin was found in and F4/80 overlapped
419 less faithfully, suggesting heterogeneity of iron regulatory mechanisms in F4/80+ macrophages,
420 an/or the presence of iron-carrying non-macrophages such as eosinophils or neutrophils.[36,37] To
421 further confirm the asociation between iron and macrophages in Aire$^{-/-}$ mice, we labelled
422 epididymides with a primary antibody for F4/80 followed by a secondary ^{172}Yb-tagged antibody,
423 and in the same sections, produced elemental maps using LA-ICP-TOF-MS. The resulting images
424 were co-registered on a per-pixel bases and showed co-localization of ^{172}Yb-positive pixels with
425 the ^{56}Fe signature, strongly suggesting that macrophages are the source of excess intracellular iron
426 (**Fig. 6D**).
427
428 Excess iron in tissues could lead to reactive oxygen species through the Fenton reaction,[38–40] and
429 in turn could cause DNA damage. Therefore, we measured DNA fragmentation in sperm isolated
430 from caudal epididymis of *Aire*$^{+/+}$ or *Aire*$^{+/-}$ and *Aire*$^{-/-}$ males using the comet assay, which reveals
431 single- and double-stranded breaks in the DNA. We found an increased percentage of sperm
432 containing DNA damage, as revealed by "comet tails" in *Aire*$^{-/-}$ samples compared to controls (**Fig.**
433 **7;** *Aire*$^{+/+}$, 2.35 ± 0.92% vs. *Aire*$^{-/-}$, 7.98 ± 3.69).
434
435 **Decreased concentrations of Cu, Zn, and Se also correlate with increased sperm DNA**
436 **fragmentation in *Aire*$^{-/-}$ animals**
437 Oxidative stress due to increased reactive oxygen species (ROS) can result in DNA damage in
438 cells.[41,42] Because sperm are transcriptionally inert, they do not possess the ability for *de novo*
439 synthesis of antioxidants and thus are especially prone to oxidative damage. To protect the sperm
440 from such assault, the epididymal epithelial cells secrete antioxidant enzymes - glutathione

441 peroxidases (Gpxs) and peroxiredoxins - into the luminal compartment[12,19,43] for which essential
442 elements such as Cu, Zn, and Se are of core structural component. To test this, we measured the
443 concentration of metals from the caput, corpus, and cauda epididymis using ICP-QQQ-MS.
444 Compared to *Aire*$^{+/+}$ and *Aire*$^{-/-}$*;Rag1*$^{-/-}$ samples, concentrations of Cu, Zu, and Se were reduced,
445 particularly in cauda epididymis of *Aire*$^{-/-}$ animals **(Supplemental Fig. 2, A-E).** Elemental analysis
446 by LA-ICP-TOF-MS corroborated the findings for ^{63}Cu and ^{64}Zn, which were strikingly reduced
447 in *Aire*$^{-/-}$ epididymis as compared to that of *Aire*$^{+/+}$ controls.
448

449 **Discussion**

450 Male-factor infertility, which accounts for about half of these cases, can stem from several
451 problems, including underlying autoimmune disease. In this instance, autoreactive lymphocytes
452 may target the generative sources of male germ cells – the testis and epididymis – perturbing sperm
453 maturation and negatively impacting fertility. We previously showed that male mice deficient in
454 *Aire*, the transcription factor critical for establishing self-antigen specific tolerance to developing
455 T cells in the thymus, suffered from subfertility with increased infiltration of CD3+ T cells into
456 the testis and generation of anti-testis and anti-epididymal antibodies.[10] Here, we report increased
457 numbers of activated T cells and macrophages within the epididymis, which was associated with
458 disruptions in inorganic physiology and sperm DNA damage.
459

460 We derived an *Aire*-deficient mouse model by targeting exon 2 of *Aire* using CRISPR/Cas9
461 technology. These mice recapitulated prior findings of *Aire* deficiency, in that both endocrine and
462 non-endocrine organs showed evidence of autoimmunity as well as severe male subfertility.
463 Importantly, the absence of adaptive immune cells, achieved by crossing Aire-deficient mice to

464 *Rag1*-deficient mice, completely restored fertility. This observation conclusively demonstrates
465 that infertility in *Aire*$^{-/-}$ males is driven by the presence of autoreactive lymphocytes rather than a
466 germ cell or reproductive tract intrinsic role for Aire.
467
468 In many animals, we found high numbers of CD4+ and CD8+ T cells, as well as B cells, in the
469 epididymis of *Aire*$^{-/-}$ males, while we did not observe testicular abnormalities. This result suggests
470 that infertility may arise from impaired epididymal function. Using immunohistochemistry, we
471 found that T cell abundance varied between animals but also showed as age- and region-specific
472 differences in the epididymis. Additionally, flow cytometry revealed increased proportions of
473 activated (CD69+) CD8+ T cells in all segments of the epididymis of *Aire*$^{-/-}$ animals. While CD44
474 expression was high on nearly all T cells regardless of genotype, the late activation marker, CD25,
475 was upregulated in only CD4+ T cells from caudal *Aire*$^{-/-}$ epididymis, possibly indicating a
476 memory phenotype in this region. Together, these data suggest that Aire deficiency promotes
477 activation of CD8+ and CD4+ T cells, potentially due to chronic interaction between the T cell
478 receptor and self-antigens presented in the context of MHC class I or class II in the Aire$^{-/-}$
479 epididymal environment. Future experiments will include additional markers that will reveal
480 memory and exhaustion phenotypes of these cells.
481
482 In addition to characterizing the immune cell infiltrates, we set out to understand the potential
483 mechanism of fibrosis in autoimmune-mediated epididymitis by combining immunohistochemical
484 staining and mass spectrometry mapping of the metal content using LA-ICP-TOF-MS and ICP-
485 QQQ-MS. While epididymal fibrosis is a hallmark feature of inflamed epididymis due to infection
486 or experimentally induced autoimmune epididymitis,[44,45] our findings of interstitial iron overload
487 as well as ferritin-positive interstitial macrophages are reminiscent of hemochromatosis and

488 bleomycin-induced idiopathic pulmonary fibrosis where the associations between iron,
489 macrophages, and fibrosis are well-established.[31,33,46–48] It should be recognized that, although
490 macrophages likely account for most F4/80+ cells, other cells express this marker (eg, a subset of
491 dendritic cells[49], and eosinophils[36]) and thus may also be responsible for carrying iron.
492 Conversely, ferritin+/F480-negative cells may also account for excess iron in the Aire$^{-/-}$
493 epididymides. Dysregulation of iron chemistry can promote oxidative damage through Fenton
494 reaction and increase hydroxyl radicals that readily cause cellular DNA damage, which may
495 instigate fragmentation of sperm DNA and fibrosis of the interstitium through the wound healing
496 process. While the sequence of events – whether accumulation of iron promotes fibrosis such as
497 that observed in the lung[48] or vice versa[33] – is unknown, we surmise that the autoimmune injury
498 to the epididymis activates F4/80+ interstitial macrophages evidenced by their morphological
499 changes, which by working together with myofibroblasts, promotes fibrosis of the epididymal
500 interstitium.[50]
501
502 We show that autoimmune-mediated epididymitis decreases the concentrations of essential metals
503 in the epididymis, including Cu, Zn, and Se. These findings were surprising because imbalance of
504 these elements in seminal fluid is associated with sperm abnormality and infertility in humans,[51,52]
505 To protect the sperm from oxidative damage, the epididymal epithelial cells express a wide variety
506 of antioxidant enzymes including Cu-Zn superoxide dismutases (including SOD1 and SOD3[53]),
507 glutathione peroxidases (Gpxs[11,54–56]), and thioredoxin-glutathione reductase (i.e. TXNRD3[57]).
508 These enzymes have been shown to be released into the lumen in the form of epididymosomes by
509 the epithelial cells.[58] Deficiency of these essential cofactors may confer deleterious effect on the
510 activity of key antioxidant enzymes including SODs and selenoproteins TXNRD3, Gpx1, 3, and

511 4, exposing sperm to reactive oxygen species-mediated oxidative stress and DNA damage.[59,60] We
512 speculate that decreases in Cu, Zn, and Se lead to defects in antioxidant enzyme production or
513 function, resulting in sperm DNA damage. While further studies are required to confirm levels of
514 antioxidant activity and production of reactive oxygen species, this model provides a plausible
515 explanation for why sperm from *Aire*$^{-/-}$ males fail to allow embryo progression to blastocyst stage
516 upon *in vitro* fertilization.[60,61]
517
518 In summary, we demonstrate that Aire deficiency and resultant autoimmune attack to the
519 epididymis disrupts inorganic physiology of the epididymis, in particular accumulation of Fe in
520 the interstitial space, and decreases in Zn, Se, Cu, which may in turn promote increased ROS
521 production and damage to sperm DNA. Interstitial macrophages as well as myofibroblasts likely
522 play a significant role in the fibrogenesis using similar mechanisms found in the liver and the
523 lung.[62] Based on the results from *Aire*$^{-/-}$*;Rag1*$^{-/-}$ animals, we demonstrate that fibrogenesis, Fe
524 accumulation, and Zn, Cu and Se depletion in the interstitium require the presence of adaptive
525 immune cells. Future studies will focus on further characterizing these immune population in the
526 *Aire*$^{-/-}$ epididymis to delineate how they participate in the fibrogenic transformation of the
527 epididymis and promote imbalance of essential metals that are critical to maintain male fertility.
528 Further studies are necessary to understand the mechanisms that contribute to decreases in essential
529 metals such as Se, Cu, and Zn in autoimmune-mediated subfertility.
530

531 **Acknowledgements**

532 We thank Dr. Lindsay Moritz and Dr. Sue Hammoud at University of Michigan for the provision
533 of the comet assay protocol. Metal analysis using ICP-QQQ-MS and LA-ICP-TOF-MS was

performed at the Quantitative Bio Element Analysis and Mapping Center (QBEAM) located at Michigan State University, East Lansing, MI, USA. Figures were created using BioRender.

References

1. *Infertility Prevalence Estimates, 1990–2021. Geneva: World Health Organization.*; 2023.
2. Practice Committee of the American Society for Reproductive Medicine. Diagnostic evaluation of the infertile male: a committee opinion. *Fertil Steril*. 2015;103(3):e18-25.
3. Sharma A, Minhas S, Dhillo WS, Jayasena CN. Male infertility due to testicular disorders. *J Clin Endocrinol Metab*. 2021;106(2):e442-e459.
4. Hamada A, Esteves SC, Agarwal A. Unexplained male infertility. *Hum Androl*. 2011;1(1):2-16.
5. Finelli R, Leisegang K, Finocchi F, De Masi S, Agarwal A, Damiani G. The impact of autoimmune systemic inflammation and associated medications on male reproductive health in patients with chronic rheumatological, dermatological, and gastroenterological diseases: A systematic review. *Am J Reprod Immunol*. 2021;85(5):e13389.
6. Anderson MS, Venanzi ES, Klein L, et al. Projection of an immunological self shadow within the thymus by the aire protein. *Science*. 2002;298(5597):1395-1401.
7. Ahonen P, Myllärniemi S, Sipilä I, Perheentupa J. Clinical variation of autoimmune polyendocrinopathy–candidiasis–ectodermal dystrophy (APECED) in a series of 68 patients. *N Engl J Med*. 1990;322(26):1829-1836.
8. Eisenbarth GS, Gottlieb PA. Autoimmune polyendocrine syndromes. *N Engl J Med*. 2004;350(20):2068-2079.
9. Michels AW, Gottlieb PA. Autoimmune polyglandular syndromes. *Nat Rev Endocrinol*. 2010;6(5):270-277.
10. Warren BD, Ahn SH, Brittain KS, et al. Multiple lesions contribute to infertility in males lacking autoimmune regulator. *Am J Pathol*. 2021;191(9):1592-1609.
11. Hinton BT, Palladino MA, Rudolph D, Lan ZJ, Labus JC. The role of the epididymis in the protection of spermatozoa. *Curr Top Dev Biol*. 1996;33:61-102.
12. O'Flaherty C. Orchestrating the antioxidant defenses in the epididymis. *Andrology*. 2019;7(5):662-668.
13. Gervasi MG, Visconti PE. Molecular changes and signaling events occurring in spermatozoa during epididymal maturation. *Andrology*. 2017;5(2):204-218.

567 14. Fournier-Delpech S, Colas G, Courot M. The first cleavage of tubal sheep eggs after
568 fertilization with epididymal or ejaculated spermatozoa. *C R Seances Acad Sci III*.
569 1981;292(7):515-517.

570 15. Rinaldi VD, Donnard E, Gellatly K, et al. An atlas of cell types in the mouse epididymis and
571 vas deferens. *Elife*. 2020;9.

572 16. Dacheux JL, Gatti JL, Dacheux F. Contribution of epididymal secretory proteins for
573 spermatozoa maturation. *Microsc Res Tech*. 2003;61(1):7-17.

574 17. Da Silva N, Shum WWC, Breton S. Regulation of vacuolar proton pumping ATPase-
575 dependent luminal acidification in the epididymis. *Asian J Androl*. 2007;9(4):476-482.

576 18. Carr DW, Usselman MC, Acott TS. Effects of pH, lactate, and viscoelastic drag on sperm
577 motility: A species Comparison1. *Biol Reprod*. 1985;33(3):588-595.

578 19. Ingold I, Aichler M, Yefremova E, et al. Expression of a catalytically inactive mutant form of
579 glutathione peroxidase 4 (Gpx4) confers a dominant-negative effect in male fertility. *J Biol*
580 *Chem*. 2015;290(23):14668-14678.

581 20. Chabory E, Damon C, Lenoir A, et al. Epididymis seleno-independent glutathione peroxidase
582 5 maintains sperm DNA integrity in mice. *J Clin Invest*. Published online June 22, 2009.

583 21. Dou Q, Turanov AA, Mariotti M, et al. Selenoprotein TXNRD3 supports male fertility via the
584 redox regulation of spermatogenesis. *J Biol Chem*. 2022;298(8):102183.

585 22. Bettger WJ. Zinc and selenium, site-specific versus general antioxidation. *Can J Physiol*
586 *Pharmacol*. 1993;71(9):721-724.

587 23. Hamilton LE, Oko R, Miranda-Vizuete A, Sutovsky P. Sperm redox system equilibrium:
588 Implications for fertilization and male fertility. *Adv Exp Med Biol*. 2022;1358:345-367.

589 24. Zee DZ, MacRenaris KW, O'Halloran TV. Quantitative imaging approaches to understanding
590 biological processing of metal ions. *Curr Opin Chem Biol*. 2022;69(102152):102152.

591 25. Albus U. Guide for the Care and Use of Laboratory Animals (8th edn). *Lab Anim*.
592 2012;46(3):267-268.

593 26. Ding D, Liu J, Dong K, et al. PNLDC1 is essential for piRNA 3′ end trimming and transposon
594 silencing during spermatogenesis in mice. *Nat Commun*. 2017;8(1).

595 27. Croy A, Yamada AT, Demayo FJ, Adamson SL. *The Guide to Investigation of Mouse*
596 *Pregnancy*. Elsevier Gezondheidszorg; 2018.

597 28. Paton C, Hellstrom J, Paul B, Woodhead J, Hergt J. Iolite: Freeware for the visualisation and
598 processing of mass spectrometric data. *J Anal At Spectrom*. 2011;26(12):2508.

599 29. Jasti S, Warren BD, McGinnis LK, Kinsey WH, Petroff BK, Petroff MG. The autoimmune
600 regulator prevents premature reproductive senescence in female mice. *Biol Reprod*.
601 2012;86(4):110.

602 30. Tai Y, Woods EL, Dally J, et al. Myofibroblasts: Function, formation, and scope of molecular
603 therapies for skin fibrosis. *Biomolecules*. 2021;11(8):1095.

604 31. Mehta KJ, Farnaud SJ, Sharp PA. Iron and liver fibrosis: Mechanistic and clinical aspects.
605 *World J Gastroenterol*. 2019;25(5):521-538.

606 32. Kowdley KV. Iron overload in patients with chronic liver disease. *Gastroenterol Hepatol (N*
607 *Y)*. 2016;12(11):695-698.

608 33. Ali MK, Kim RY, Brown AC, et al. Critical role for iron accumulation in the pathogenesis of
609 fibrotic lung disease. *J Pathol*. 2020;251(1):49-62.

610 34. Wendisch D, Dietrich O, Mari T, et al. SARS-CoV-2 infection triggers profibrotic
611 macrophage responses and lung fibrosis. *Cell*. 2021;184(26):6243-6261.e27.

612 35. Munro HN, Linder MC. Ferritin: structure, biosynthesis, and role in iron metabolism. *Physiol*
613 *Rev*. 1978;58(2):317-396.

614 36. McGarry MP, Stewart CC. Murine eosinophil granulocytes bind the murine macrophage-
615 monocyte specific monoclonal antibody F4/80. *J Leukoc Biol*. 1991;50(5):471-478.

616 37. Sasmono RT, Ehrnsperger A, Cronau SL, et al. Mouse neutrophilic granulocytes express
617 mRNA encoding the macrophage colony-stimulating factor receptor (CSF-1R) as well as
618 many other macrophage-specific transcripts and can transdifferentiate into macrophages in
619 vitro in response to CSF-1. *J Leukoc Biol*. 2007;82(1):111-123.

620 38. Bansal AK, Bilaspuri GS. Effect of ferrous sulphate and ascorbic acid on motility, viability
621 and lipid peroxidation of crossbred cattle bull spermatozoa. *Animal*. 2008;2(1):100-104.

622 39. Aitken RJ, Wingate JK, De Iuliis GN, McLaughlin EA. Analysis of lipid peroxidation in
623 human spermatozoa using BODIPY C11. *Mol Hum Reprod*. 2007;13(4):203-211.

624 40. Papanikolaou G, Pantopoulos K. Iron metabolism and toxicity. *Toxicol Appl Pharmacol*.
625 2005;202(2):199-211.

626 41. Gonzalez-Hunt CP, Wadhwa M, Sanders LH. DNA damage by oxidative stress: Measurement
627 strategies for two genomes. *Curr Opin Toxicol*. 2018;7:87-94.

628 42. Loft S. Oxidative DNA damage in human sperm influences time to pregnancy. *Hum Reprod*.
629 2003;18(6):1265-1272.

630 43. Chabory E, Damon C, Lenoir A, et al. Epididymis seleno-independent glutathione peroxidase
631 5 maintains sperm DNA integrity in mice. *J Clin Invest*. 2009;119(7):2074-2085.

632 44. Wijayarathna R, Pasalic A, Nicolas N, et al. Region-specific immune responses to
633 autoimmune epididymitis in the murine reproductive tract. *Cell Tissue Res*. 2020;381(2):351-
634 360.

635 45. Pleuger C, Ai D, Hoppe ML, et al. The regional distribution of resident immune cells shapes
636 distinct immunological environments along the murine epididymis. *Elife*. 2022;11.

637 46. Pei Z, Qin Y, Fu X, et al. Inhibition of ferroptosis and iron accumulation alleviates pulmonary
638 fibrosis in a bleomycin model. *Redox Biol*. 2022;57(102509):102509.

639 47. Misharin AV, Morales-Nebreda L, Reyfman PA, et al. Monocyte-derived alveolar
640 macrophages drive lung fibrosis and persist in the lung over the life span. *J Exp Med*.
641 2017;214(8):2387-2404.

642 48. Maus M, López-Polo V, Mateo L, et al. Iron accumulation drives fibrosis, senescence and the
643 senescence-associated secretory phenotype. *Nat Metab*. 2023;5(12):2111-2130.

644 49. Sun X, Jones HP, Dobbs N, Bodhankar S, Simecka JW. Dendritic cells are the major antigen
645 presenting cells in inflammatory lesions of murine Mycoplasma respiratory disease. *PLoS*
646 *One*. 2013;8(2):e55984.

647 50. Adler M, Mayo A, Zhou X, et al. Principles of cell circuits for tissue repair and fibrosis.
648 *iScience*. 2020;23(2):100841.

649 51. Bleau G, Lemarbre J, Faucher G, Roberts KD, Chapdelaine A. Semen selenium and human
650 fertility. *Fertil Steril*. 1984;42(6):890-894.

651 52. Nenkova G, Petrov L, Alexandrova A. Role of trace elements for oxidative status and quality
652 of human sperm. *Balkan Med J*. 2017;34(4):343.

653 53. Alvarez JG, Storey BT. Role of superoxide dismutase in protecting rabbit spermatozoa from
654 O2 toxicity due to lipid peroxidation. *Biol Reprod*. 1983;28(5):1129-1136.

655 54. Schwaab V, Faure J, Dufaure JP, Drevet JR. GPx3: the plasma-type glutathione peroxidase is
656 expressed under androgenic control in the mouse epididymis and vas deferens. *Mol Reprod*
657 *Dev*. 1998;51(4):362-372.

658 55. Noblanc A, Kocer A, Chabory E, et al. Glutathione peroxidases at work on epididymal
659 spermatozoa: An example of the dual effect of reactive oxygen species on mammalian male
660 fertilizing ability. *J Androl*. 2011;32(6):641-650.

661 56. Drevet JR. The antioxidant glutathione peroxidase family and spermatozoa: A complex story.
662 *Mol Cell Endocrinol*. 2006;250(1-2):70-79.

663 57. Wang H, Dou Q, Jeong KJ, Choi J, Gladyshev VN, Chung JJ. Redox regulation by TXNRD3
664 during epididymal maturation underlies capacitation-associated mitochondrial activity and
665 sperm motility in mice. *J Biol Chem*. 2022;298(7):102077.

666 58. Barrachina F, Ottino K, Elizagaray ML, et al. Regulatory T cells play a crucial role in
667 maintaining sperm tolerance and male fertility. *Proc Natl Acad Sci U S A*. 2023;120(37).

668 59. Lopes S M Sc, Sun JG PhD, Jurisicova A PhD, Meriano J B Sc, Casper RF MD. Sperm
669 deoxyribonucleic acid fragmentation is increased in poor-quality semen samples and
670 correlates with failed fertilization in intracytoplasmic sperm injection. *Fertil Steril*.
671 1998;69(3):528-532.

672 60. Seli E, Gardner DK, Schoolcraft WB, Moffatt O, Sakkas D. Extent of nuclear DNA damage
673 in ejaculated spermatozoa impacts on blastocyst development after in vitro fertilization. *Fertil*
674 *Steril*. 2004;82(2):378-383.

675 61. Lawler T, Parlato L, Warren Andersen S. Racial disparities in colorectal cancer
676 clinicopathological and molecular tumor characteristics: a systematic review. *Cancer Causes*
677 *Control*. Published online September 9, 2023.

678 62. Chung S, Overstreet JM, Li Y, et al. TGF-β promotes fibrosis after severe acute kidney injury
679 by enhancing renal macrophage infiltration. *JCI Insight*. 2018;3(21).

680

681 **Figure Legends**

682 **Figure 1. Aire-deficient (*Aire*$^{-/-}$) males develop autoimmunity towards non-reproductive and**
683 **reproductive organs and are subfertile.** (A) Immunofluorescence of Aire in *Aire*$^{-/-}$ and *Aire*$^{+/+}$
684 thymi. AF488 (green), Aire; AF568 (red), Cytokeratin 14 (K14, mTEC marker); DAPI (blue),
685 nuclei. Asterisks highlight areas in which additional Aire^{+} cells can be seen outside the inset. Note
686 the absence of the characteristic intranuclear speckles in the *Aire*$^{-/-}$ thymus. Scale bar = 10µm. (B)
687 Representative hematoxylin and eosin-stained lung, salivary gland, prostate, and cauda epididymis
688 sections from 20 week-old *Aire*$^{-/-}$ and *Aire*$^{+/+}$ males. Lung: n=3 per genotype; prostate: *Aire*$^{-/-}$,
689 n=11/*Aire*$^{+/+}$, n=7; caudal epididymis: n=11 per genotype. Arrows point to lymphoid aggregates.
690 Scale bars = 100µm. (C) Fertility outcomes of *Aire*$^{-/-}$ and *Aire*$^{+/+}$ males on the *Rag1*-sufficient or -
691 deficient background. ANOVA followed by Tukey's post hoc test. ns: $P>0.05$, *$PP < 0.0001$.

692 **Figure 2. Immune cell infiltrates consisting of CD4+ T cells, CD8+ T cells and CD19+ B cells**
693 **occur early and persist with age in *Aire*$^{-/-}$ epididymides.** (A) Immunohistochemical staining for
694 CD4+ T cells, CD8+ T cells and CD19+ B cells in the epididymis of 19-20 week old *Aire*$^{+/+}$ and
695 A*Aire*$^{-/-}$ epididymides. CD4+ and CD8+ T cells are also found sporadically in the *Aire*$^{+/+}$
696 epididymis (arrows). *Aire*$^{+/+}$(19-20 weeks: n=5), and *Aire*$^{-/-}$ (19-20 weeks: n=7), Scale bar = 50
697 µm. (B) Photomicrograph of the three main anatomical regions of the epididymis (Caput, H;
698 Corpus; B; Cauda; T). (C, D) Manually enumerated CD4+ (*Aire*$^{+/+}$: n=8; *Aire*$^{-/-}$: n=9) and CD8+
699 (*Aire*$^{+/+}$: n=10, *Aire*$^{-/-}$: n=12) T cells in the epididymis. Red dots denote 19-20 week old animals;
700 black dots denote 7-9 week old animals. Statistical Analysis: Wilcoxon non-parametric t-test. ns:
701 $p>0.05$, *$PP<0.01$.

702 **Figure 3. Flow cytometric analysis of CD4+ and CD8+ T cells from *Aire*$^{-/-}$ and *Aire*$^{+/+}$**
703 **epididymides.** (A) Gating strategy for flow cytometric assessment of lymphocyte population in
704 the epididymis. FSC-A: forward scatter area, SSC-A: side scatter area, FSC-H: forward scatter
705 height. Epididymides were separated into Caput-Corpus and Cauda, digested into single cell
706 suspensions, and analyzed by flow cytometry for the expression of CD25, CD44, and CD69. (B)
707 Relative abundance of CD45hi cells in *Aire*$^{+/+}$ and *Aire*$^{-/-}$ epididymides; (C) Relative abundance
708 of CD45hi B220+ cells in the epididymis; (D, F) Relative abundance of CD45hi CD4+T, followed
709 by CD4+CD25+ CD4+CD44+, and CD4+CD69+ T cells in the epididymis; (E,G) Relative
710 abundance of CD45hi CD8+ T cells, followed by CD8+CD25+, CD8+CD44+, and CD8+CD69+
711 T cells in the epididymis. Animals analyzed were 19-20 weeks old. Wilcoxon t-test, ns: $P>0.05$,
712 *$P< 0.01$.

713 **Figure 4. Fibrotic changes in epididymides of *Aire*$^{-/-}$ males.** Masson's trichrome staining reveals
714 extensive fibrosis (blue staining) in the interstitium of *Aire*$^{-/-}$ epididymides of 9-10 weeks and 19-
715 20-week-old males compared to that of *Aire*$^{+/+}$ and *Aire*$^{-/-}$;*Rag1*$^{-/-}$ controls. Shown are the cauda
716 and portions of the corpus epididymis. Scale bar = 1000μm.

717 **Figure 5. ^{56}Fe concentration is increased in the *Aire*$^{-/-}$ epididymis and localizes to the**
718 **interstitium. (A)** ICP-QQQ-MS analysis of epididymal segments. Red = 7-9 wks, Black = 19-20
719 wks. **(B)** ^{56}Fe measurement in sperm using ICP-QQQ-MS. **(C)** LA-ICP-TOF-MS reveals the
720 spatial distribution of ^{56}Fe to the interstitium of the *Aire*$^{+/+}$ (n=3 for each age), *Aire*$^{-/-}$ (n=4 for
721 each age), and *Aire*$^{-/-}$;*Rag1*$^{-/-}$ (n=4 for 9-10wks, n=3 for 19-20wks) epididymis. Statistical
722 analysis: Kruskal-Wallis One-Way ANOVA followed by Dunn-Bonferroni post-hoc was
723 conducted to compare the means of each group for (A). Wilcoxon-test for (B). ****$P<0.00005$,
724 ns = not significant.

725 **Figure 6. F4/80+ macrophages carry intracellular ferritin-associated iron in the interstitium**
726 **of *Aire*$^{-/-}$ epididymis. (A)** Representative immunohistochemical staining for F4/80+ macrophages
727 in cauda epididymides of *Aire*$^{-/-}$ compared to *Aire*$^{+/+}$ and *Aire*$^{-/-}$*;Rag1*$^{-/-}$ *mice. Aire*$^{+/+}$(7-10 weeks:
728 n=4, 19-20 weeks: n=5), *Aire*$^{-/-}$ (7-10 weeks: n= 4, 19-20 weeks: n=7), and *Aire*$^{-/-}$*;Rag1*$^{-/-}$ (7-10
729 weeks: n=4, 19-20 weeks: n=3) Scale bar = 100 µm. **(B)** Immunofluorescence staining for F4/80+
730 (Alexa Fluor 488, green) and CD163+ (Alexa Fluor 546, red) macrophages in *Aire*$^{+/+}$ and *Aire*$^{-/-}$
731 epididymal tail. Scale bar = 50 µm. **(C)** Dual immunofluorescence staining for F4/80 (Alexa Fluor
732 488, green) and ferritin (Alexa Fluor 546, red) in *Aire*$^{+/+}$ and *Aire*$^{-/-}$ cauda epididymis. Scale bar =
733 100 µm. (**(D)** Representative LA-ICP-TOF-MS images of *Aire*$^{-/-}$ epididymis stained with F4/80
734 primary antibody followed by a secondary antibody tagged to a lanthanide (^{172}Yb) revealing
735 colocalization of ^{56}Fe with F4/80+ macrophages. Scale bar = 1000µm.

736 **Figure 7. Comet assay reveal increased DNA fragmentation in caudal sperm from *Aire*$^{-/-}$**
737 **males.** Epididymal tail sperm from *Aire*$^{+/+}$ or *Aire*$^{+/-}$ and *Aire*$^{-/-}$ males aged between 7 to 20 weeks
738 were processed for comet analysis. Scale bar = 1000µm *p = 0.048, paired t-test.

739 **Supplementary Table 1.** Elemental concentration in the gelatin standards determined by ICP-
740 QQQ-MS.
741
742 **Supplementary Table 2.** LA-ICP-TOF-MS parameters.

743 **Supplementary Figure 1**. αSMA+ myofibroblasts abound in the interstitium of *Aire*$^{-/-}$ cauda
744 epididymis in comparison to *Aire*$^{+/+}$ epididymis of similar age. Scale bar = 200 µm for top and
745 bottom row; 50 µm for middle row

746 **Supplementary Figure 2. Concentrations of ^{63}Cu and ^{64}Zn are decreased in *Aire*$^{-/-}$**

747 **epididymis. (A-C)** ICP-QQQ-MS analysis of individual segments of the epididymis show

748 regional decreases in ^{63}Cu, ^{64}Zn, and ^{78}Se in the *Aire*$^{-/-}$ epididymis compared to *Aire*$^{+/+}$ or *Aire*$^{-}$

749 $^{/-}$*;Rag1*$^{-/-}$. Red = 7-9 weeks old, Black = 19-20 weeks old. Elemental distribution of ^{63}Cu

750 Statistical analysis: Kruskal-Wallis One-Way ANOVA followed by Dunn-Bonferroni post-hoc

751 was conducted to compare the means of each group. *p**(D)** and ^{64}Zn **(E)** in 20-week-old *Aire*$^{+/+}$

752 and *Aire*$^{-/-}$ epididymis using LA-ICP-TOF-MS; Se abundance was below the detection limit of

753 this technology. Scale bar = 1000 μm.

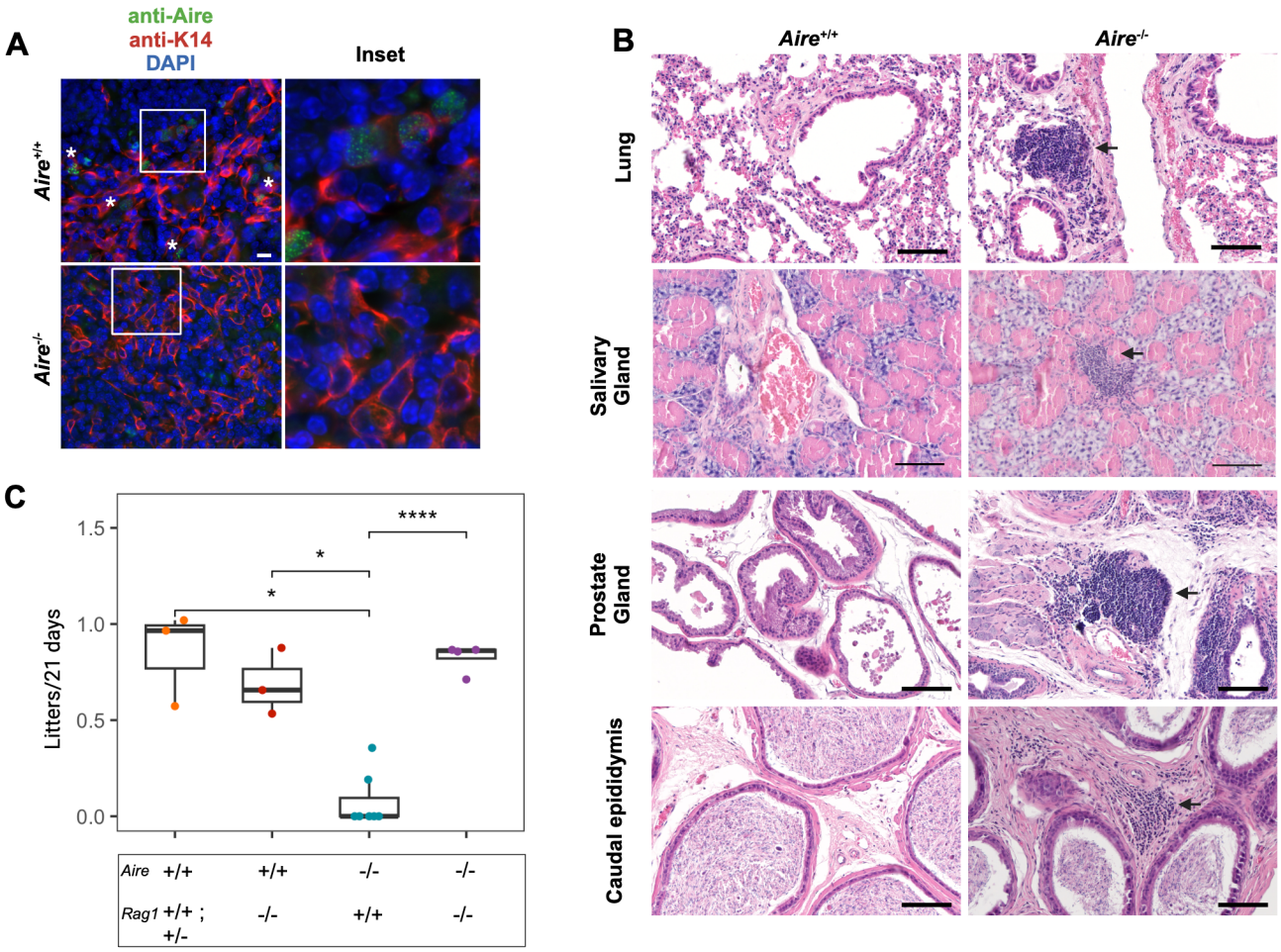
A
anti-Aire
anti-K14
DAPI
Inset
Aire+/+
Aire-/-
B
Aire+/+
Aire-/-
Lung
Salivary Gland
Prostate Gland
Caudal epididymis
C
Litters/21 days
1.5
1.0
0.5
0.0
*
*
****
Aire +/+ +/+ -/- -/-
Rag1 +/+ ; +/- -/- +/+ -/-

Figure 1. **Aire-deficient (*Aire*$^{-/-}$) males develop autoimmunity towards non-reproductive and reproductive organs and are subfertile. (A)** Immunofluorescence of Aire in *Aire*$^{-/-}$ and *Aire*$^{+/+}$ thymi. AF488 (green), Aire; AF568 (red), Cytokeratin 14 (K14, mTEC marker); DAPI (blue), nuclei. Asterisks highlight areas in which additional Aire^{+} cells can be seen outside the inset. Note the absence of the characteristic intranuclear speckles in the *Aire*$^{-/-}$ thymus. Scale bar = 10µm. **(B)** Representative hematoxylin and eosin-stained lung, salivary gland, prostate, and cauda epididymis sections from 20 week-old *Aire*$^{-/-}$ and *Aire*$^{+/+}$ males. Lung: n=3 per genotype; prostate: *Aire*$^{-/-}$, n=11/*Aire*$^{+/+}$, n=7; caudal epididymis:n=11 per genotype. Arrows point to lymphoid aggregates. Scale bars = 100 µm. **(C)** Fertility outcomes of *Aire*$^{-/-}$ and *Aire*$^{+/+}$ males on the *Rag1*-sufficient or -deficient background. ANOVA followed by Tukey's post hoc test. ns: $P>0.05$, *$P<0.05$, ****$P < 0.0001$.

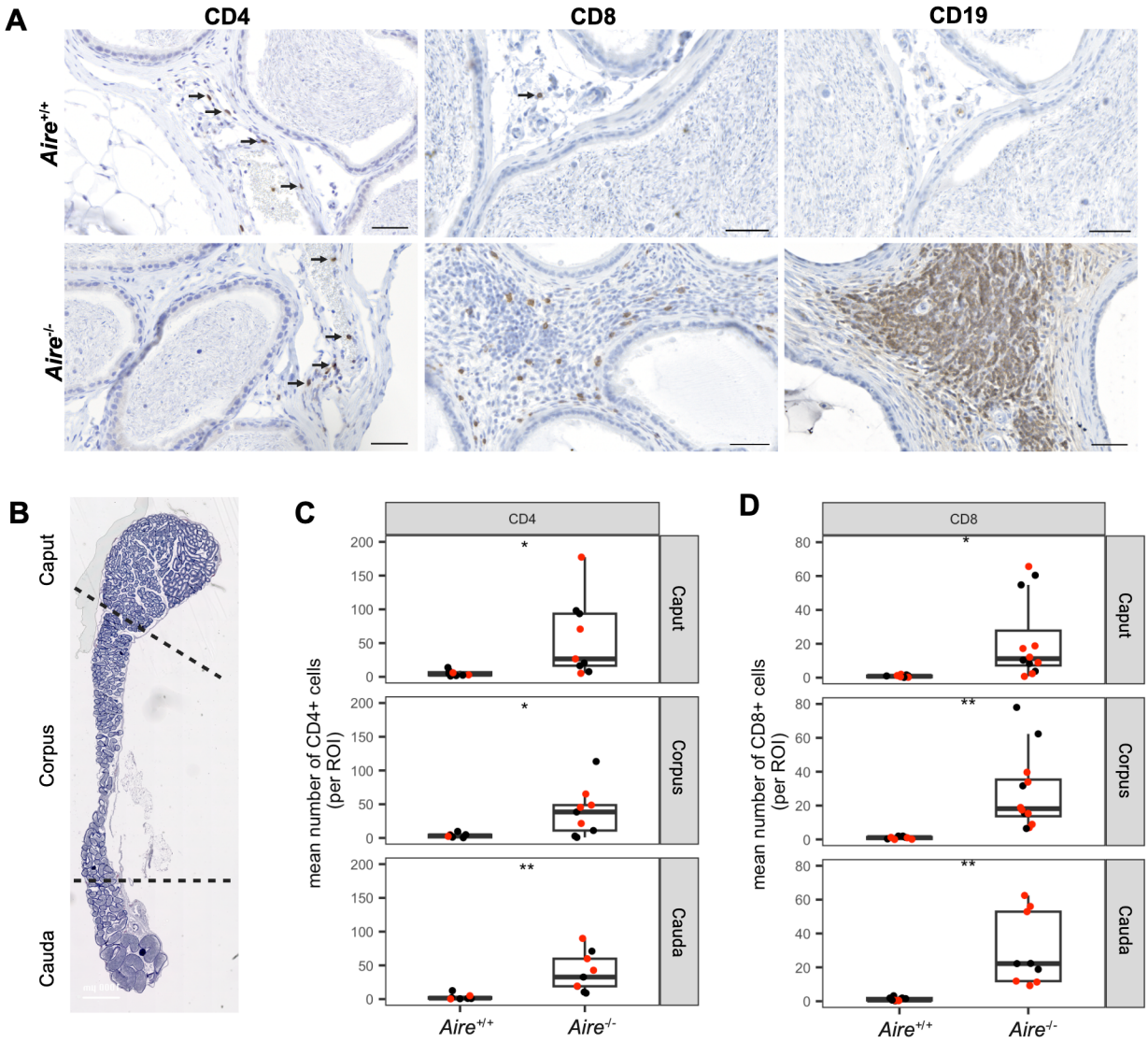
A
CD4
CD8
CD19
Aire+/+
Aire-/-
B
Caput
Corpus
Cauda
C
CD4
mean number of CD4+ cells (per ROI)
Caput
Corpus
Cauda
Aire+/+
Aire-/-
D
CD8
mean number of CD8+ cells (per ROI)
Caput
Corpus
Cauda
Aire+/+
Aire-/-

Figure 2. Immune cell infiltrates consisting of CD4+ T cells, CD8+ T cells and CD19+ B cells occur early and persist with age in *Aire*$^{-/-}$ epididymides. (A) Immunohistochemical staining for CD4+ T cells, CD8+ T cells and CD19+ B cells in the epididymis of 19-20 week old *Aire*$^{+/+}$ and A*ire*$^{-/-}$ epididymides. CD4+ and CD8+ T cells are also found sporadically in the *Aire*$^{+/+}$ epididymis (arrows). *Aire*$^{+/+}$(19-20 weeks: n=5) ,and *Aire*$^{-/-}$ (19-20 weeks: n=7), Scale bar = 50 µm. **(B)** Photomicrograph of the three main anatomical regions of the epididymis (Caput, H; Corpus; B; Cauda; T). **(C, D)** Manually enumerated CD4+ (*Aire*$^{+/+}$: n=8; *Aire*$^{-/-}$: n=9) and CD8+ (*Aire*$^{+/+}$: n=10, *Aire*$^{-/-}$: n=12) T cells in the epididymis. Red dots denote 19-20 week old animals; black dots denote 7-9 week old animals. Statistical Analysis: Wilcoxon non-parametric t-test. ns: $p>0.05$, *$P<0.05$, **$P<0.01$.

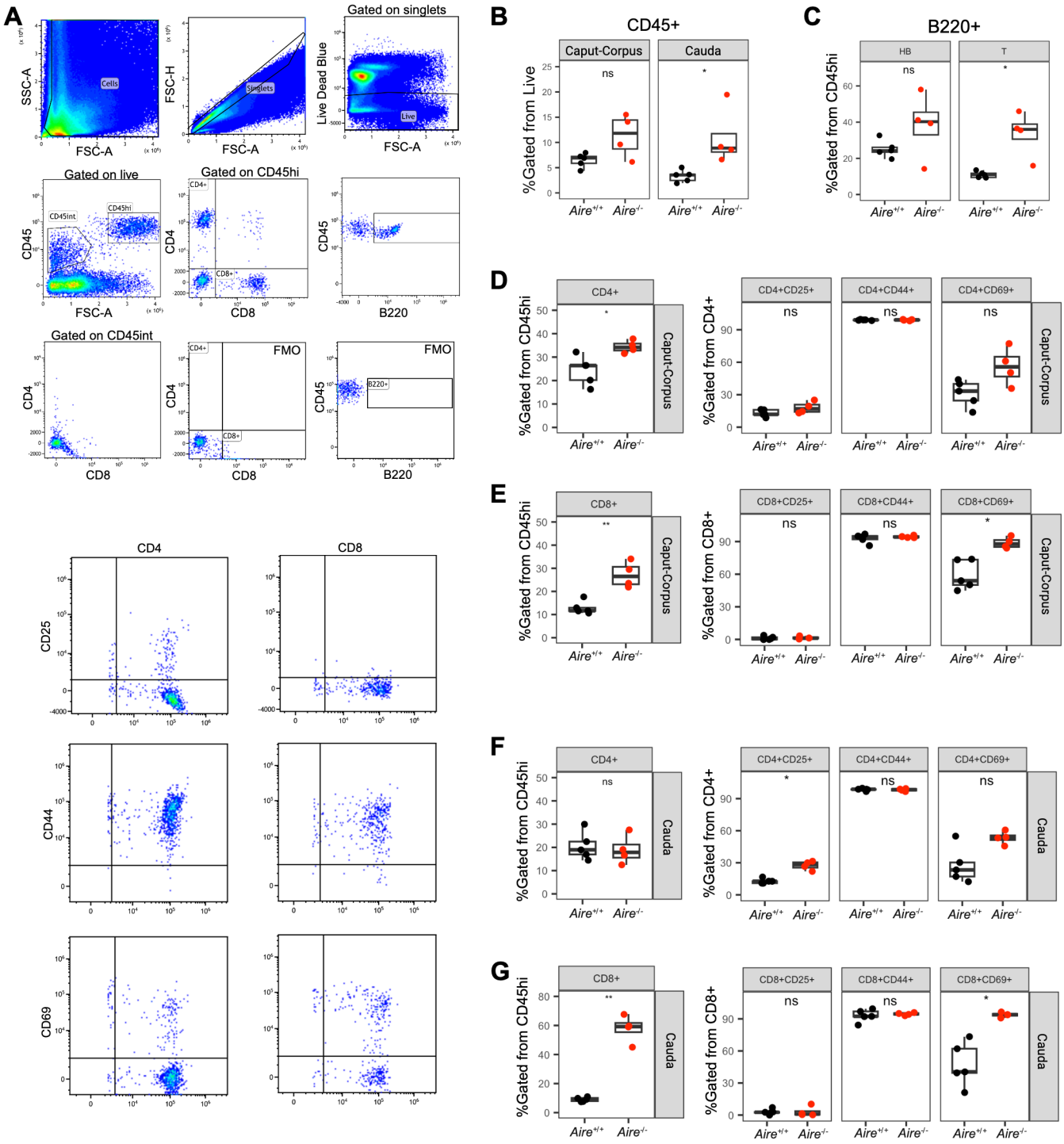
A
SSC-A
FSC-A
Cells
FSC-H
Singlets
Gated on singlets
Live Dead Blue
Live
Gated on live
CD45int
CD45hi
CD45
Gated on CD45hi
CD4+
CD8+
CD4
CD8
B220
Gated on CD45int
FMO
B220+
CD25
CD44
CD69
B
CD45+
Caput-Corpus
Cauda
%Gated from Live
ns
*
Aire+/+
Aire-/-
C
B220+
HB
T
%Gated from CD45hi
D
CD4+
CD4+CD25+
CD4+CD44+
CD4+CD69+
%Gated from CD4+
E
CD8+
CD8+CD25+
CD8+CD44+
CD8+CD69+
%Gated from CD8+
F
G

Figure 3. Flow cytometric analysis of CD4+ and CD8+ T cells from *Aire*$^{-/-}$ and *Aire*$^{+/+}$ epididymides. (A) Gating strategy for flow cytometric assessment of lymphocyte population in the epididymis. FSC-A: forward scatter area, SSC-A: side scatter area, FSC-H: forward scatter height. Epididymides were separated into Caput-Corpus and Cauda, digested into single cell suspensions, and analyzed by flow cytometry for the expression of CD25, CD44, and CD69. **(B)** Relative abundance of CD45hi cells in *Aire*$^{+/+}$ and *Aire*$^{-/-}$ epididymides; **(C)** Relative abundance of CD45hi B220+ cells in the epididymis; **(D, F)** Relative abundance of CD45hi CD4+T, followed by CD4+CD25+ CD4+CD44+, and CD4+CD69+ T cells in the epididymis; **(E,G)** Relative abundance of CD45hi CD8+ T cells, followed by CD8+CD25+, CD8+CD44+, and CD8+CD69+ T cells in the epididymis. Wilcoxon t-test, ns: $P>0.05$, *$P<0.05$, **$p < 0.01$.

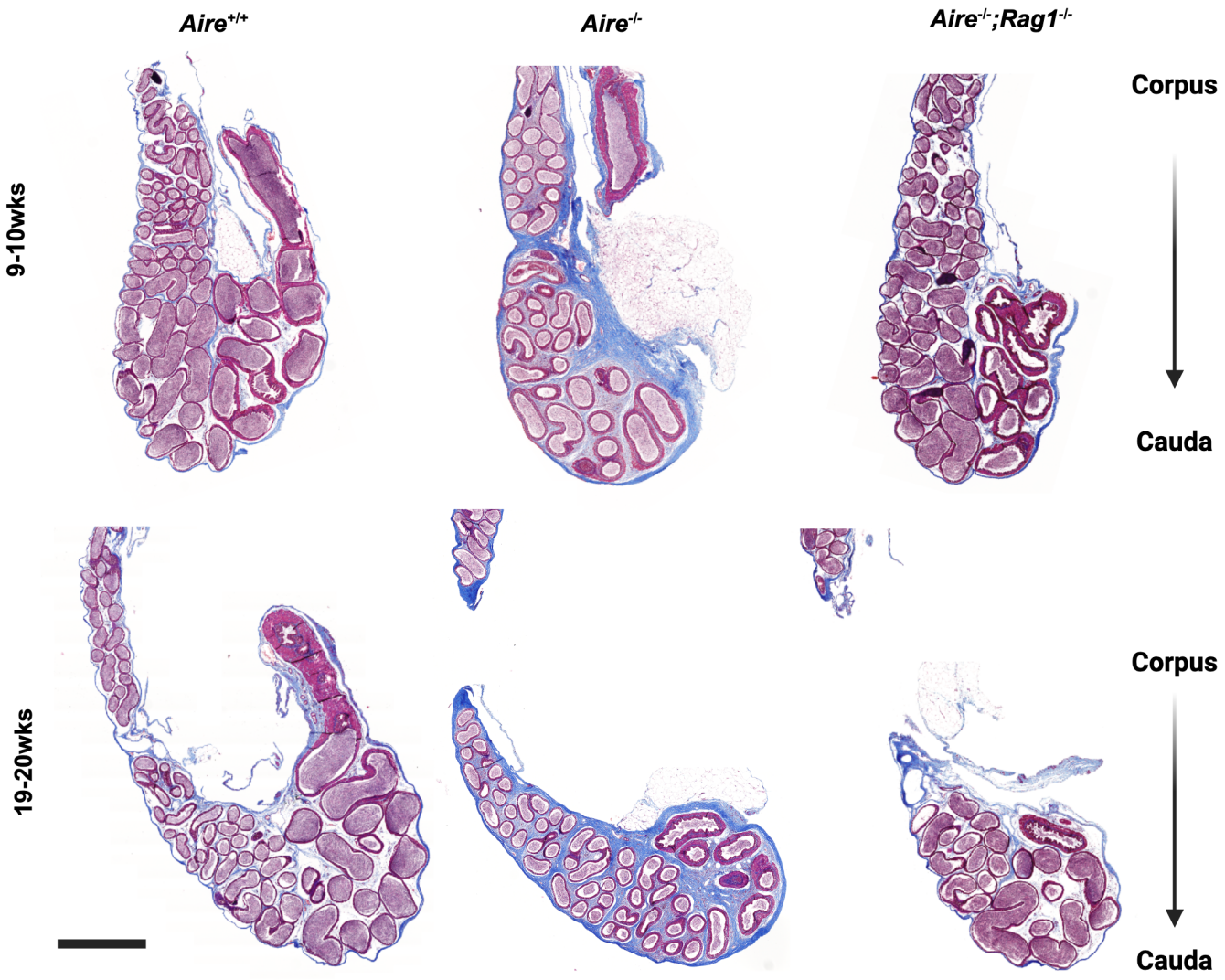
Aire+/+
Aire-/-
Aire-/-;Rag1-/-
9-10wks
19-20wks
Corpus
Cauda
Corpus
Cauda

Figure 4. Masson's trichrome staining reveals extensive fibrosis (blue staining) in the interstitium of *Aire*$^{-/-}$ epididymides of 9-10 weeks and 19-20-week-old males compared to that of *Aire*$^{+/+}$ and *Aire*$^{-/-}$*;Rag1*$^{-/-}$ controls. Shown are the cauda and portions of the corpus epididymis. Scale bar = 1000 μm.

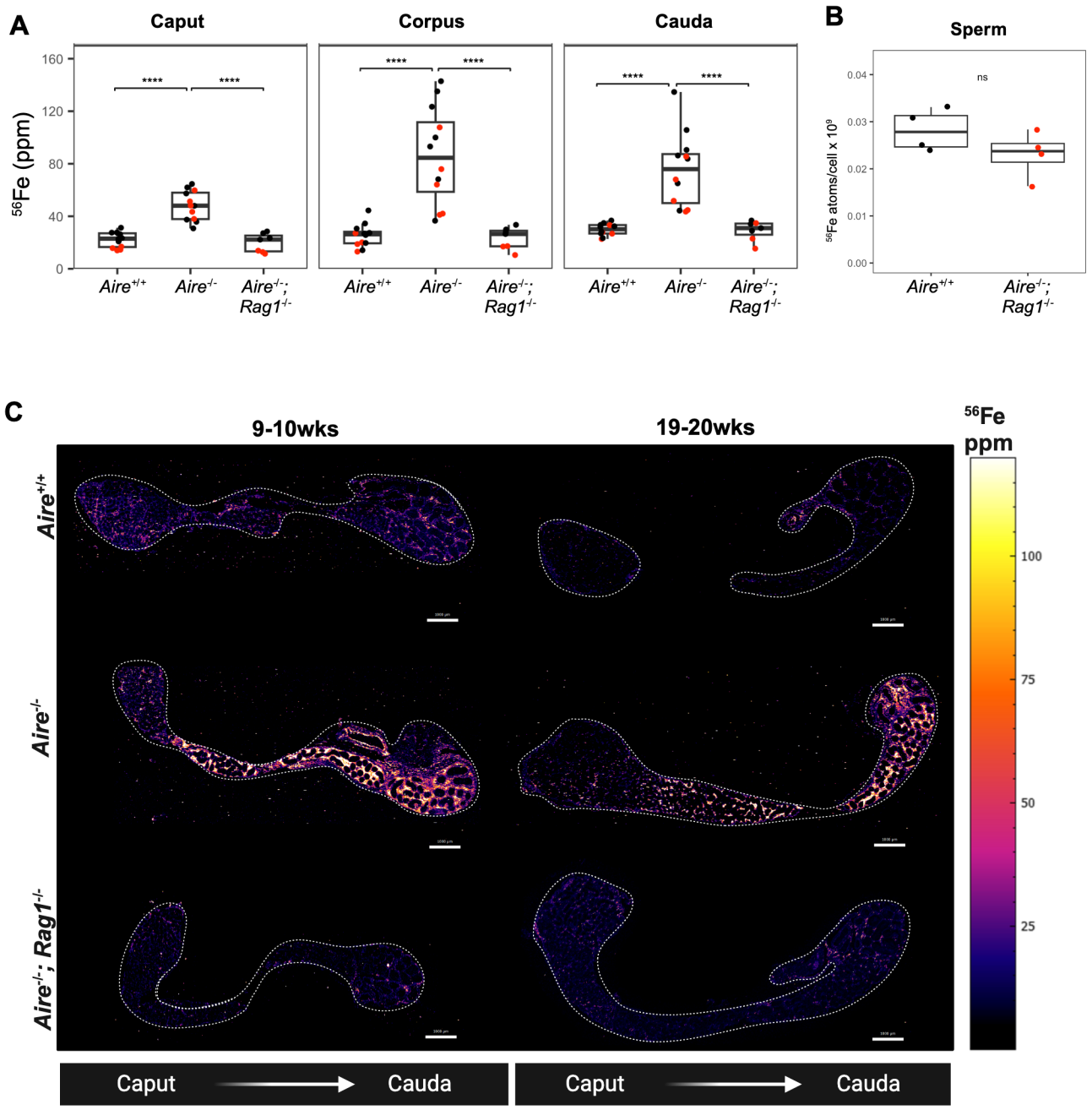
A
Caput
Corpus
Cauda
^{56}Fe (ppm)
160
120
80
40
0
****
Aire+/+
Aire-/-
Aire-/-; Rag1-/-
B
Sperm
^{56}Fe atoms/cell x 10^{9}
0.04
0.03
0.02
0.01
0.00
ns
C
9-10wks
19-20wks
^{56}Fe ppm
100
75
50
25
Caput
Cauda

Figure 5. ^{56}Fe concentration is increased in the *Aire*$^{-/-}$ epididymis and localizes to the interstitium. (A) ICP-QQQ-MS analysis of epididymal segments. Red = 7-9 wks, Black = 19-20 wks. **(B)** ^{56}Fe measurement in sperm using ICP-QQQ-MS. **(C)** LA-ICP-TOF-MS reveals the spatial distribution of ^{56}Fe to the interstitium of the *Aire*$^{+/+}$ (n=3 for each age), *Aire*$^{-/-}$ (n=4 for each age), and *Aire*$^{-/-}$*;Rag1*$^{-/-}$ (n=4 for 9-10wks, n=3 for 19-20wks) epididymis. Statistical analysis: Kruskal-Wallis One-Way ANOVA followed by Dunn-Bonferroni post-hoc was conducted to compare the means of each group for (A). Wilcoxon-test for (B). ****P<0.00005, ns = not significant.

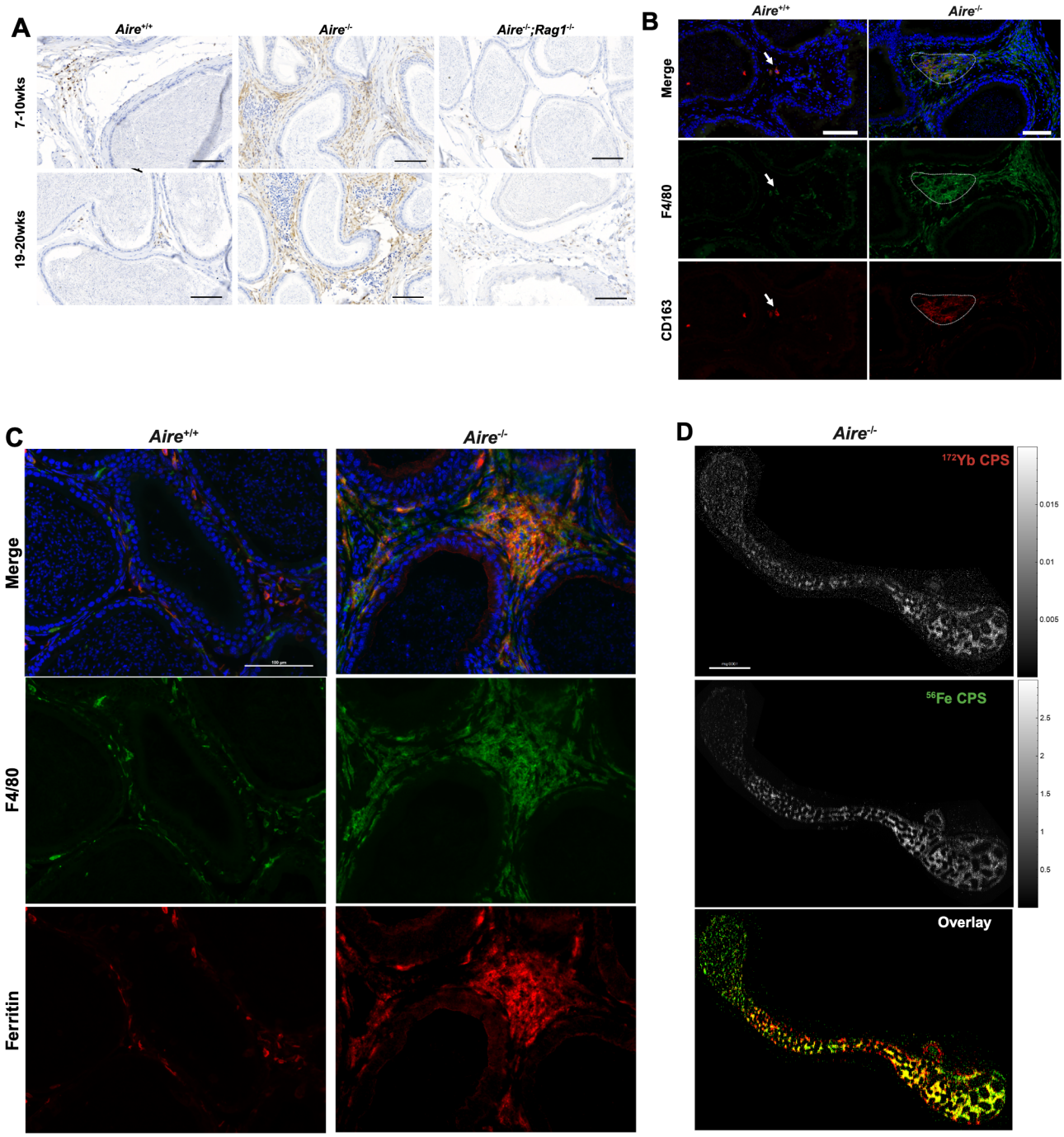
A
Aire+/+
Aire-/-
Aire-/-;Rag1-/-
7-10wks
19-20wks
B
Aire+/+
Aire-/-
Merge
F4/80
CD163
C
Aire+/+
Aire-/-
Merge
F4/80
Ferritin
D
Aire-/-
172Yb CPS
0.015
0.01
0.005
56Fe CPS
2.5
2
1.5
1
0.5
Overlay

Figure 6. F4/80+ macrophages carry intracellular ferritin-associated iron in the interstitium of *Aire*$^{-/-}$ epididymis. (A) Representative immunohistochemical staining for F4/80+ macrophages in cauda epididymides of *Aire*$^{-/-}$ compared to *Aire*$^{+/+}$ and *Aire*$^{-/-}$*;Rag1*$^{-/-}$ *mice. Aire*$^{+/+}$(7-10 weeks: n=4, 19-20 weeks: n=5), *Aire*$^{-/-}$ (7-10 weeks: n= 4, 19-20 weeks: n=7), and *Aire*$^{-/-}$*;Rag1*$^{-/-}$ (7-10 weeks: n=4, 19-20 weeks: n=3) Scale bar = 100 µm. **(B)** Immunofluorescence staining for F4/80+ (Alexa Fluor 488, green) and CD163+ (Alexa Fluor 546, red) macrophages in *Aire*$^{+/+}$ and *Aire*$^{-/-}$ epididymal tail. Scale bar = 50 µm. **(C)** Dual immunofluorescence staining for F4/80 (Alexa Fluor 488, green) and ferritin (Alexa Fluor 546, red) in *Aire*$^{+/+}$ and *Aire*$^{-/-}$ cauda epididymis. Scale bar = 100 µm. (**D)** Representative LA-ICP-TOF-MS images of *Aire*$^{-/-}$ epididymis stained with F4/80 primary antibody followed by a secondary antibody tagged to a lanthanide (^{172}Yb) revealing colocalization of ^{56}Fe with F4/80+ macrophages. Scale bar = 1000 µm.

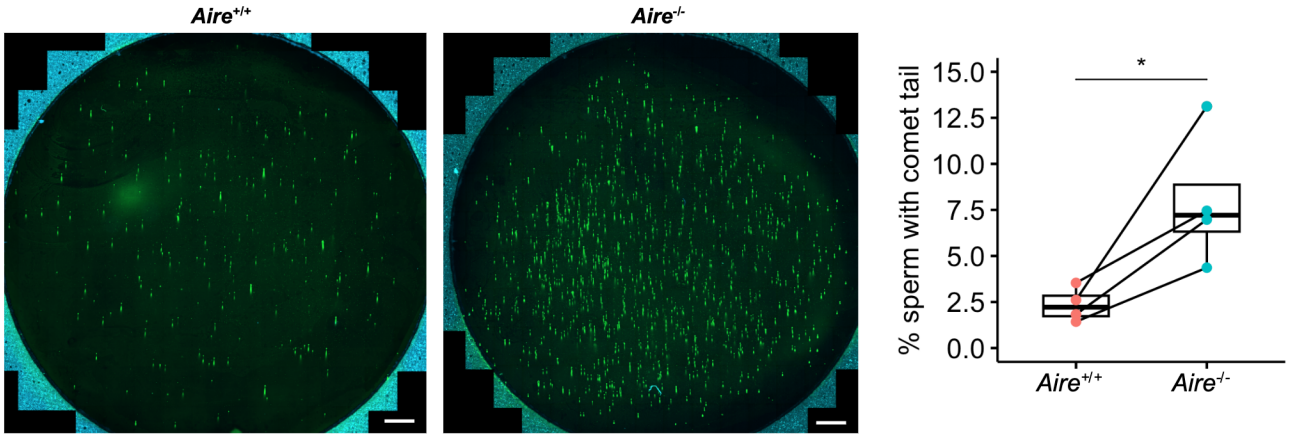
Aire+/+
Aire-/-
% sperm with comet tail
15.0
12.5
10.0
7.5
5.0
2.5
0.0
*
Aire+/+
Aire-/-

Figure 7. Comet assay reveal increased DNA fragmentation in caudal sperm from *Aire*$^{-/-}$ males. Epididymal tail sperm from *Aire*$^{+/+}$ or *Aire*$^{+/-}$ and *Aire*$^{-/-}$ males aged between 7 to 20 weeks were processed for comet analysis. Scale bar = 1000 µm *p = 0.048, paired t-test.

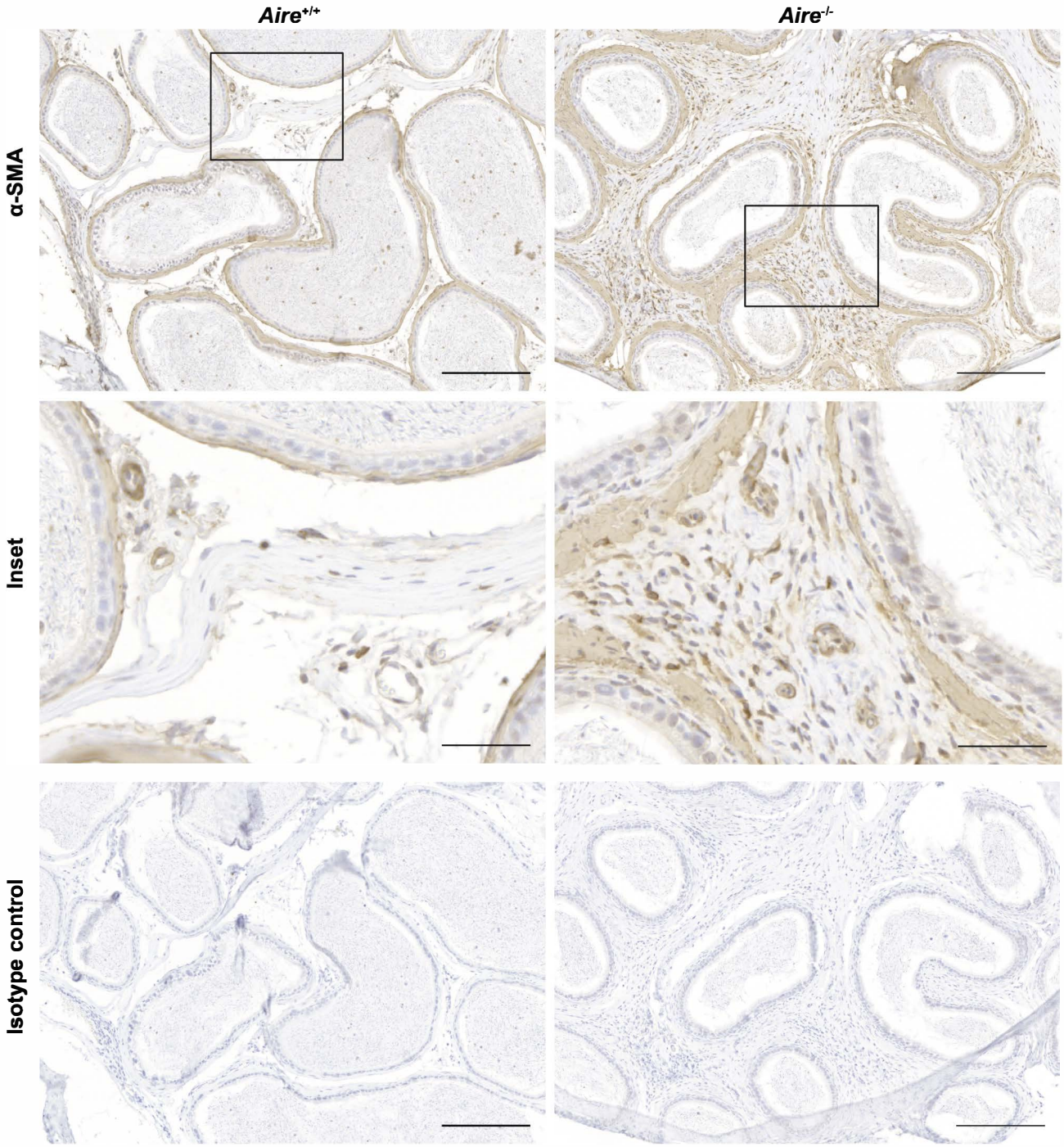

Supplemental Figure 1. αSMA+ myofibroblasts abound in the interstitium of *Aire*$^{-/-}$ cauda epididymis in comparison to *Aire*$^{+/+}$ epididymis of similar age. Scale bar = 200 μm for top and bottom row; 50 μm for middle row

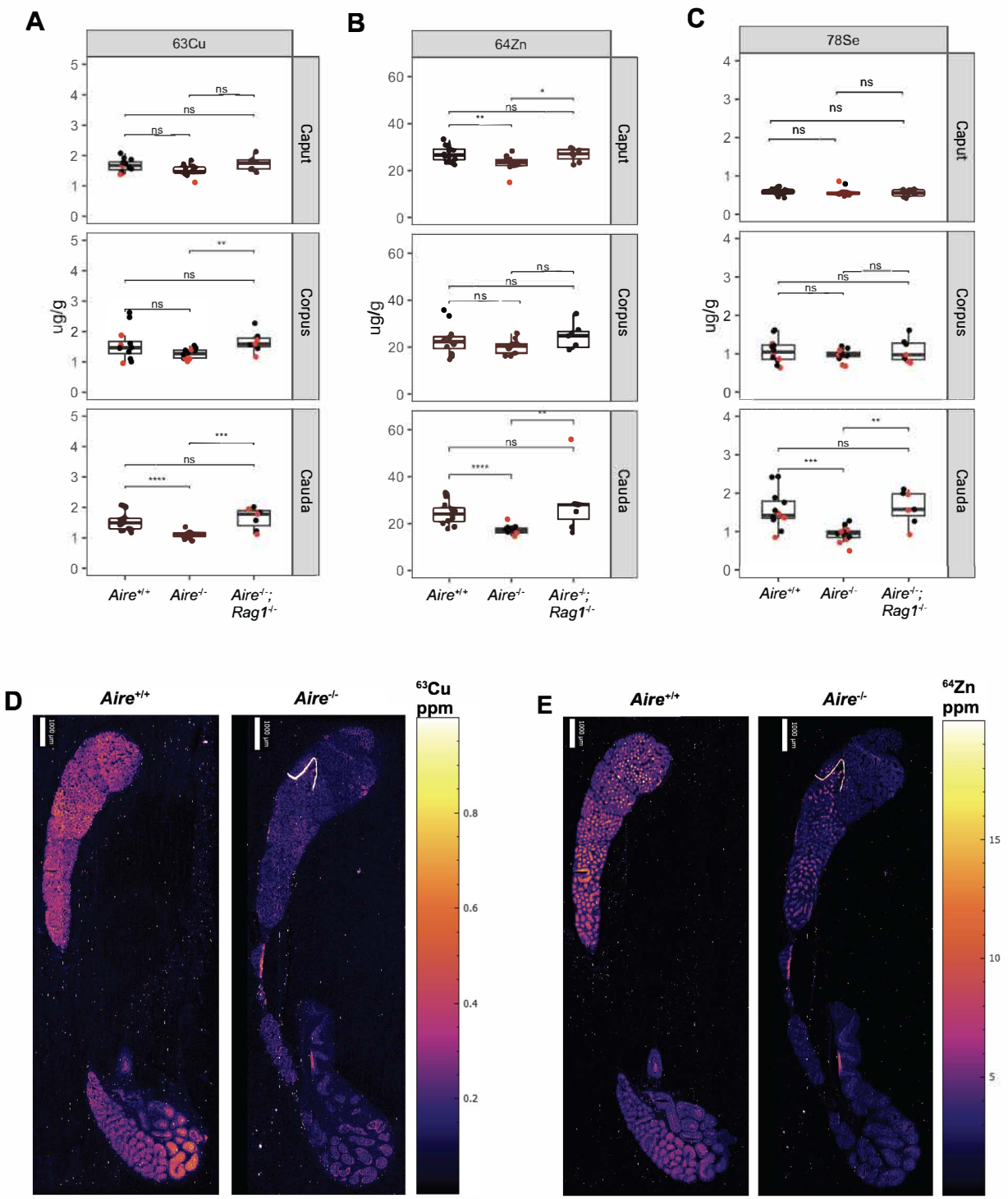

Supplementary Figure 2. Concentrations of ^{63}Cu and ^{64}Zn are decreased in *Aire*$^{-/-}$ epididymis. (A-C) ICP-QQQ-MS analysis of individual segments of the epididymis show regional decreases in ^{63}Cu, ^{64}Zn, and ^{78}Se in the *Aire*$^{-/-}$ epididymis compared to *Aire*$^{+/+}$ or *Aire*$^{-/-}$;*Rag1*$^{-/-}$. Red = 7-9 weeks old, Black = 19-20 weeks old. Elemental distribution of ^{63}Cu Statistical analysis: Kruskal-Wallis One-Way ANOVA followed by Dunn-Bonferroni post-hoc was conducted to compare the means of each group. *p<0.05, **p<0.005, ***p<0.0005, ****p<0.00005. **(D)** and ^{64}Zn **(E)** in 20-week-old *Aire*$^{+/+}$ and *Aire*$^{-/-}$ epididymis using LA-ICP-TOF-MS; Se abundance was below the detection limit of this technology. Scale bar = 1000 µm.

Supplementary Table 1. Elemental concentration in the gelatin standards

Sample Name	^{24}Mg	^{44}Ca	^{55}Mn	^{57}Fe	^{58}Ni	^{63}Cu	^{64}Zn
Gelatin Blank	2.106	0.916	0	0.679	0.013	0.030	0.096
Gelatin 50 ppm	53.32	44.85	55.40	56.99	56.55	56.93	55.02
Gelatin 20 ppm	26.62	21.17	26.39	26.97	27.03	27.64	26.34
Gelatin 10 ppm	14.38	11.01	13.66	14.14	14.01	14.13	13.08
Gelatin 5 ppm	8.512	6.498	7.535	8.074	7.409	7.821	7.243
Gelatin 1 ppm	3.460	2.113	1.681	2.564	1.768	1.832	1.776

Supplementary Table 2. LA-ICP-TOF-MS parameters

ICP-MS Paramters (Tofwerk S2)		
Parameter	**Unit**	**Value**
RF Power	W	1550
Sampling Depth	mm	4.9
Cone Material	Nickel	-
Cone Insert (STD)	mm	3.5
Plasma Gas Flow	L/min	14.0
Auxillary Gas Flow	L/min	8.0
Nebulizer Gas Flow	L/min	0.95-1.01
Measurement Mode	CCT Mode	-
CCT Gas Flow (100% He)	mL/min	5
CCT Focus lens	V	-19.5
CCT Entry Lens	V	-180
CCT Mass	V	250
CCT Bias	V	10
CCT Exit Lens	V	-200
Time-of-Flight Parameters (Tofwerk S2)		
Parameter	**Unit**	**Value**
m/z range	amu	14 - 256
Resolution	m/Δm	1000
ODG Settings	ms	24
Notch Bias	V	-80
Notch (40 amu)	V	1.6
Notch (36 amu)	V	1
Notch (28 amu)	V	2
Notch (15.8 amu)	V	2
Laser Ablation Parameters (ESL Bioimage 266 nm)		
Parameter	**Unit**	**Value**
Spot Size	µm	10
Interline Distance (y)	µm	10
Overlap (x)	µm	0
Repetition Rate	Hz	100
Laser Power	%	60
Laser Fluence	J/cm^2	15

Sample Energy	mJ	0.010-0.015
Imaging Cup Flow Rate (He)	mL/min	200
Imaging Chamber Flow Rate (He)	mL/min	250
PEEK Tubing I.D.	mm	0.75